J. Fluid Mech. (2008), *vol.* 600, *pp.* 201–233.
doi:10.1017/S0022112008000438 Printed in the United Kingdom

A sphere in a uniformly rotating or shearing flow

J. J. BLUEMINK[1], D. LOHSE[1], A. PROSPERETTI[1,2] AND L. VAN WIJNGAARDEN[1]

[1]Faculty of Science and Technology and J. M. Burgers Centre for Fluid Dynamics, University of Twente, P.O. Box 217, 7500 AE Enschede, The Netherlands

[2]Department of Mechanical Engineering, The John Hopkins University Baltimore, MD 21218, USA

(Received 13 November 2006 and in revised form 17 December 2007)

It is known that, in a linear shear flow, fluid inertia causes a particle to spin more slowly than the surrounding fluid. The present experiments performed with a sphere with fixed centre, but free to rotate in a fluid undergoing solid-body rotation around a horizontal axis indicate that the spin rate of the sphere can be larger than that of the flow when the sphere is sufficiently far from the axis. Numerical simulations at Reynolds number $5 \leqslant Re \leqslant 200$ confirm this observation. To gain a better understanding of the phenomenon, the rotating flow is decomposed into two shear flows along orthogonal directions. It is found numerically that the cross-stream shear has a much stronger effect on the particle spin rate than the streamwise shear. The region of low stress at the back of the sphere is affected by the shear component of the incident flow. While for the streamwise case the shift is minor, it is significant for cross-stream shear. The results are interpreted on the basis of the effect of the shear flow components on the quasi-toroidal vortex attached in the sphere's near wake. The contributions of streamwise and cross-stream shear to the particle spin can be linearly superposed for $Re = 20$ and 50.

1. Introduction

The behaviour of particles or bubbles in a flow is one of the most fundamental problems of fluid mechanics. While a considerable body of knowledge exists in the limits of vanishing Reynolds numbers (see e.g. Lamb 1932; Happel & Brenner 1965; Kim & Karrila 1991) or inviscid flow (see e.g. Lamb 1932; Milne-Thompson 1968; Auton, Hunt & Prud'homme 1988), the investigation of finite-Reynolds-number effects has been limited to simple situations such as steady uniform or shearing flows. Even for these relatively simple configurations, however, our understanding is far from complete.

The complexity of the general problem suggests that a profitable way to proceed is to consider a variety of flows with well-defined characteristics in the hope of building a broadly applicable synthesis. Rotational flows, which are studied in the present paper, are particularly interesting in view of their widespread occurrence. It appears impossible, for example, to achieve a satisfactory description of particle dispersion in turbulence, or of the behaviour of fluidized beds, in the absence of a good understanding of the drag and lift forces in such flows.

Here we study the behaviour of a sphere in a fluid undergoing solid-body rotation (see figure 1*a*). The centre of the sphere is fixed while it is allowed to rotate in a torque-free state. Experimentally, the situation is realized by placing a buoyant sphere

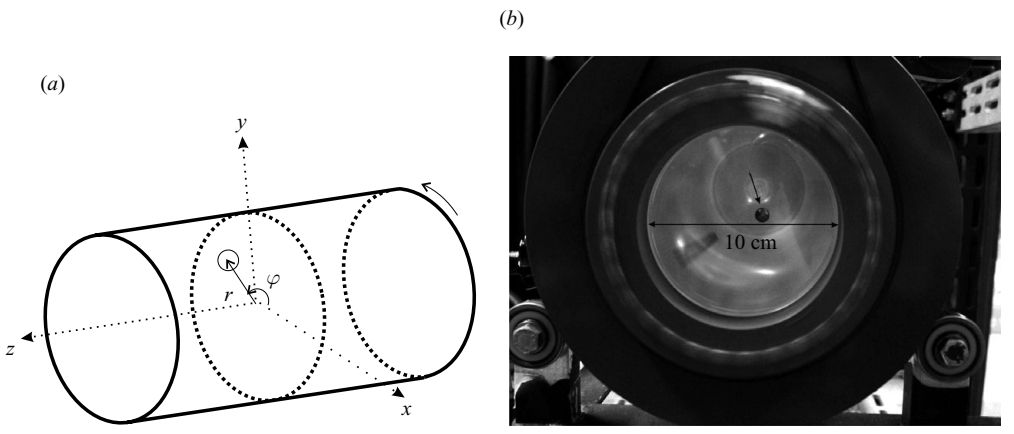

FIGURE 1. Sphere in solid-body rotation: (*a*) geometry, gravity in the *y*-direction, (*b*) a sphere (indicated by the arrow) in its equilibrium position in the small cylinder.

in a liquid-filled cylinder rotating around a horizontal axis (see figure 1*b*) and results up to Reynolds numbers $Re \simeq 800$ are shown, with

$$Re = \frac{2RU_0}{\nu}. \tag{1.1}$$

In this equation R is the sphere radius, U_0 the undisturbed flow velocity at the sphere centre and ν the fluid viscosity. Numerically, we determine and explain the dependence of the particle spin rate and lift force on the Reynolds number Re up to 200 and study the effects of the individual streamwise and cross-stream components from which the motion of a fluid in solid-body rotation can be synthesized. We find that streamwise and cross-stream shear have very different effects on the particle spin. For solid-body rotation, the only other study we are aware of in which the particle is allowed to freely rotate at sizeable Reynolds number is Bagchi & Balachandar (2002*b*), whose results, however, are quite different from ours. In particular, their conclusion that the particle spin rate is never greater than that of the ambient fluid is at variance with our experiments and calculations and for the time being remains unexplained.

Earlier work on rotating flows includes Herron, Davis & Bretherton (1975) and Gotoh (1990) who calculated the hydrodynamic force acting on a sphere immersed in a rotating flow at low Reynolds number. The lift force in a rotational inviscid flow – in which, of course, the flow does not induce any rotation of the sphere – has been investigated in Lighthill (1956), Auton (1987) and Auton *et al.* (1988) (see also Drew & Lahey 1987). For the case of bubbles, Naciri (1992) and Sridhar & Katz (1995) studied experimentally situations similar to the one considered here and measured a lift coefficient considerably larger than that predicted by the available theories. Similar results have more recently been reported in van Nierop *et al.* (2007). As discussed in that paper, in the low Reynolds number limit, the hydrodynamic force appears to be very sensitive to the flow type.

Several authors have studied the trajectory of particles in fluids in solid-body rotation. Experimental results have been reported by, for example, Roberts, Kornfeld & Fowlis (1991) and Mullin *et al.* (2005). Annamalai & Cole (1986), Raju & Meiburg (1997), Gao, Ayyaswamy & Ducheyne (1997) and Coimbra & Kobayashi (2002) have studied the problem theoretically, and an analysis of the stable equilibrium points at

low Reynolds number has been given by Paradisi & Tampieri (2001), Coimbra & Kobayashi (2002) and Kobayashi & Coimbra (2005). A brief study of the equivalent problem for bubbles was presented by Lohse & Prosperetti (2003).

Our focus is on the particle spin and, therefore, quite different from that of all these authors. Furthermore, most of the previously cited theoretical papers treated the particles as points using parameterizations of the hydrodynamic force while we actually calculate it from first principles by solving the Navier–Stokes equations.

Two other classes of flows involving particle spin or fluid rotation have been studied. In one of them, the particle translates in the direction of the rotational axis of the fluid (Childress 1964; Weisenborn 1985; Kim & Choi 2002; Wang, Lu & Zhuang 2004; Candelier, Angilella, & Souhar 2004, 2005). In another group of papers (Dennis, Singh & Ingham 1980; Rubinow & Keller 1961; Oesterlé & Dinh 1998; Barkla & Auchterlonie 1971) the particle spins about an axis perpendicular to the incident flow, as in the present work, but the particle angular velocity is prescribed rather than resulting from the fluid dynamic interaction as here. Generally speaking, all these papers find a strong effect of particle spin on the hydrodynamic force, and especially on the lift. However these situations are evidently different from the one considered in this paper.

Solid-body rotation can be decomposed into two shearing flows along orthogonal directions. It is therefore of interest to consider such flows. The flow field in a unidirectional simple shear is given by

$$\boldsymbol{U}(y) = 2\omega y\hat{\boldsymbol{e}}_x, \tag{1.2}$$

where $\boldsymbol{U}$ is the undisturbed fluid velocity, 2ω is the shear rate and $\hat{\boldsymbol{e}}_{\boldsymbol{x}}$ is the unit vector. If no external torque acts on the particle, its angular velocity Ω_p will eventually adjust so as to result in a vanishing hydrodynamic torque. Lin, Peery & Schowalter (1970) studied this situation for very low values of the Taylor number defined by

$$Ta = \frac{2R^2\omega}{\nu}. \tag{1.3}$$

This quantity may be considered as the ratio of the characteristic time for rotation to that for viscous diffusion and is used later as a dimensionless measure of the liquid angular velocity. The spin rate calculated by Lin *et al.* (1970) is

$$\frac{\Omega_p}{\omega} = 1 - 0.3076\,Ta^{3/2} + o\left(Ta^{3/2}\right). \tag{1.4}$$

Poe & Acrivos (1975) found experimentally that this expression is adequate provided $Ta < 0.1$. Mikulencak & Morris (2004) investigated the same situation numerically for $0 < Ta < 100$. For $Ta > 1$ a steep decrease in the spin rate was seen with the Taylor number. Thus, the particle angular velocity decreases as the fluid inertial effects, as measured by the Taylor number, increase. Note that any difference between the particle and fluid rotation rates must be due to fluid inertia which is of course an immediate consequence of Faxèn's second theorem which states that, at vanishing Reynolds number, the angular velocity Ω_p of a torque-free sphere is the same as the local angular velocity of the ambient fluid (see e.g. Happel & Brenner 1965; Kim & Karrila 1991).

The case in which the flow incident on the particle consists of the superposition of a uniform plus a streamwise shearing flow

$$\boldsymbol{U}(y) = (\omega y - U_0)\hat{\boldsymbol{e}}_x, \tag{1.5}$$

where U_0 represents the uniform flow component, has been studied by, among others, Saffman (1965) and McLaughlin (1991) for small Reynolds numbers. Saffman (1965) finds that the sphere angular velocity is not affected by the shear component to lowest order. At higher Reynolds number the numerical results of Bagchi & Balachandar (2002*b*) can be fitted by

$$\frac{\Omega_p}{\omega} = \frac{1}{2}(1 - 0.0364Re^{0.95}) \tag{1.6}$$

for $0.5 < Re \leqslant 5$ and

$$\frac{\Omega_p}{\omega} = \frac{1}{2}(1 - 0.0755Re^{0.455}) \tag{1.7}$$

for $5 \leqslant Re \leqslant 200$. Again, the particle spin rate is seen to decrease as fluid inertia increases.

In addition to the already mentioned papers by Saffman (1965) and McLaughlin (1991), several other authors have studied the forces on particles in linear shear flows. Dandy & Dwyer (1990) calculated the force on a non-rotating particle while Bagchi & Balachandar (2002*b*) allowed the particle to rotate freely as was seen in (1.6) and (1.7). At low Reynolds number, as indicated by Mei (1992), the spin rate has little effect on the lift force. This is not the case for Reynolds numbers in the intermediate range as shown e.g. by Kurose & Komori (1999), who studied a particle with a prescribed spin rate.

In this paper we study the steady-state spin rate of torque-free particles immersed in a class of flows ranging from unidirectional shear to solid-body rotation. For the latter case, we present both experimental and numerical results, while only numerical means are used for the other cases. Unexpectedly, the spin rate of a spherical particle trapped in a liquid rotating in solid-body motion is found to exceed the angular velocity of the liquid in a large part of the parameter range. The only other reports of spheres rotating faster than the fluid are in turbulent flows (e.g. Ye & Rocco 1992; Mortensen *et al.* 2007). These data however were acquired in many-particle systems and it was the mean spin that exceeded the mean angular fluid velocity. Mortensen *et al.* (2007) ascribe this to preferential particle concentration. A somewhat surprising new result in this work is that the effects of the cross-stream shear and the streamwise shear on particle spin rate and shear stress at the particle surface can be linearly superposed for the Reynolds number range studied.

2. Preliminaries

In suitable parameter ranges, a buoyant spherical particle or bubble finds an equilibrium position when inserted in a fluid-filled horizontal cylinder rotating with constant angular velocity ω as in figure 1(*a*) (see e.g. Naciri 1992; Paradisi & Tampieri 2001; Coimbra & Kobayashi 2002; Lohse & Prosperetti 2003; Bluemink *et al.* 2005; van Nierop *et al.* 2007). At this position all forces – buoyancy, drag, added mass, pressure gradient and lift – balance. While its centre remains fixed, the particle is of course free to rotate.

In addition to the particle radius, R, and density, ρ_p, the equilibrium position of the particle in a rotating liquid depends on ω, the angular velocity of the fluid, ν and ρ, the kinematic viscosity and density of the liquid, and g, the acceleration due to gravity. Two dimensionless quantities can be formed then, in addition to the Taylor

number defined in (1.3). We take

$$Ga = \frac{2R\sqrt{2R(1-\rho_p/\rho)g}}{\nu}, \qquad \frac{\rho_p}{\rho}. \tag{2.1}$$

The Galilei number Ga is a Reynolds number based on the characteristic velocity induced by gravity; its use is particularly convenient as, for a given liquid and particle radius, it is a constant.

More standard dimensionless parameters, such as the Reynolds number, can be added to the above mentioned ones to characterize the flow environment seen by the particle. Although a dependent variable, the distance r_e of the equilibrium position from the axis of rotation is important for this purpose. With $U_0 = \omega r_e$ the Reynolds number defined earlier in (1.1) becomes

$$Re = \frac{2RU_0}{\nu} = \frac{2Rr_e\omega}{\nu}. \tag{2.2}$$

We also introduce a vorticity parameter

$$Sr_\omega = \frac{2\omega R}{U_0} = \frac{2R}{r_e}. \tag{2.3}$$

Lohse & Prosperetti (2003) presented a simplified analysis of the problem using standard large-Reynolds-number expressions for the added mass and lift forces on a bubble (see (5.1)). After adjusting for the particle density and the no-slip boundary conditions at the interface, that analysis is also applicable to a solid sphere and gives the following result for r_e:

$$\frac{r_e}{2R} = \frac{2\sqrt{2}}{3}\left[\sqrt{\left(\frac{K}{C_D}\right)^4 + \left(\frac{3}{8C_D}\right)^2\left(\frac{Ga}{Ta}\right)^4} - \left(\frac{K}{C_D}\right)^2\right]^{1/2}, \tag{2.4}$$

in which C_D is the drag coefficient and $K = 2C_L - 1 - C_A$ is composed of the added mass coefficient C_A, equal to $1/2$ in potential flow, and of the lift coefficient C_L, equal to $1/2$ in inviscid flow (Auton 1987). Clearly, as $Ta \to \infty$, we have $r_e \to 0$, i.e. the particle moves towards the axis of rotation. If we approximate C_D by a constant, which is a rough estimate appropriate in the upper range of the Reynolds numbers encountered in the experiments described in the next section, for small values of Ta (2.4) gives

$$Re = \frac{r_e}{R}Ta = 2\frac{Ta}{Sr_\omega} \simeq \frac{2Ga}{\sqrt{3C_D}}\left[1 - \frac{4}{3C_D}\left(\frac{KTa}{Ga}\right)^2\right]. \tag{2.5}$$

This estimate shows that, asymptotically, Sr_ω increases proportionally to Ta (i.e. to ω), while the Reynolds number reaches the limiting value $2Ga/\sqrt{3C_D}$, which is readily seen to coincide with the terminal velocity of the particle in still fluid, as expected. Before this limit is reached, however, Re increases as the Taylor number decreases.

3. Experiment

Experiments were conducted by placing a low-density polyethylene spherical particle (density $\rho_p = 920\,\mathrm{kg\,m^{-3}}$) in a transparent liquid-filled cylinder rotating around a horizontal axis. Most of the data were taken in a 0.1 m diameter glass cylinder (see figure 1*b*) but, in order to rule out wall effects, we also took some data in a larger, 0.5 m diameter Perspex cylinder; both cylinders were 0.5 m long. The larger cylinder

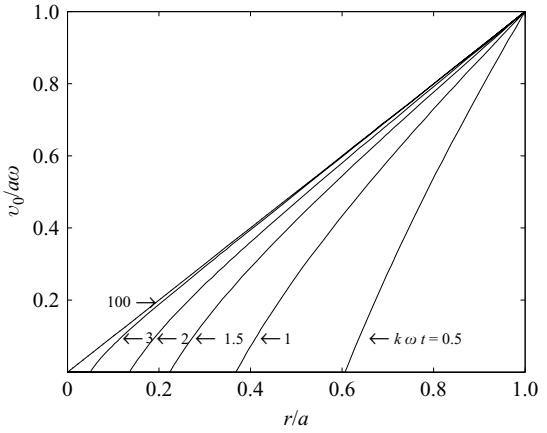

FIGURE 2. Velocity profiles for different spin-up times.

had a motor with a controlled feed-back loop which permitted setting the angular velocity with great accuracy.

Particles with radii $R = 3.1$ and 4.0 mm were used in the experiment. They were marked with paint so as to facilitate the measurement of their angular velocity from image sequences taken at a speed of 50 f.p.s. Several readings of the angular velocity of the particles and of the small cylinder were taken from each image sequence; the error bars shown in figures 3–5 represent the range of the data.

The liquids were water and a mixture of water and 75 % glycerine by weight; the dynamic viscosity of the mixture was measured with a viscometer to be $\mu = 0.0347\,\mathrm{kg\,m^{-1}\,s^{-1}}$ and the density 1180 $\mathrm{kg\,m^{-3}}$.

To be certain that the flow field as seen by the particle is solid-body rotation, sufficient time for spin-up must be allowed. In figure 2 the velocity profiles for different spin-up times for a cylinder with radius a and height h, according to Wedemeyer (1964), are shown. In the figure v_0 indicates the velocity of the fluid and it is normalized by the velocity at the cylinder wall. The time t allowed for spin-up is written in non-dimensional form as $k\omega t$, where ω is the cylinder angular velocity and $k = 0.443\ (2a)/h\sqrt{\nu/(a^2\omega)}$. For $k\omega t = 0.5$ the fluid in the cylinder is far from solid-body rotation, whereas for $k\omega t = 3$ it is quite close. The lines in the figure are valid when the viscous terms are negligible, i.e. when $ka^2\omega/\nu \gg 1$. The value of $ka^2\omega/\nu$ is indeed much larger than 1, so the above estimate is valid. For a maximum error of 1 % in velocity compared to the velocity field for solid body rotation, the spin-up time t_s for a fluid in a rotating cylinder starting from rest can be estimated to be of the order of (see e.g. Wedemeyer 1964)

$$t_s = \frac{10.3954}{\omega}\sqrt{\frac{a^2\omega}{\nu}}\,\frac{h}{2a}. \tag{3.1}$$

For the liquids used in this experiment, this relation gives estimates of a maximum spin-up time of 4 min in water and 6 min in the glycerin–water mixture for both cylinders. Data were taken well past these waiting periods. Furthermore, in several cases, two sets of data were taken an hour or so apart, letting the cylinder rotate in the intervening time; no differences (beyond the usual experimental fluctuations) were found.

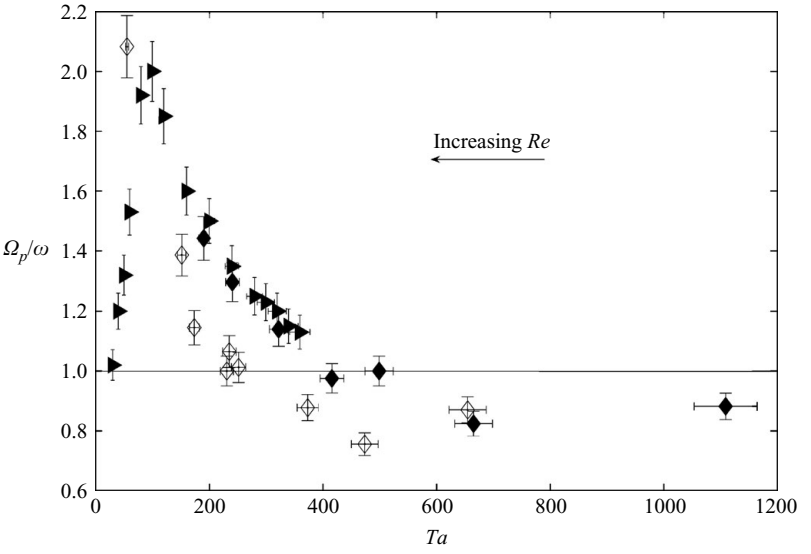

FIGURE 3. Particle spin rate Ω_p normalized by the liquid angular velocity ω versus $Ta = 2\omega R^2/\nu$ for the experiments in water. The diamonds are data from the smaller cylinder, triangles from the larger cylinder. The filled and open symbols are for particles of radius 4.0 mm and 3.1 mm, respectively. The particle Reynolds number corresponding to these data is in the range of 200 to 1000.

For experiments performed in water, the Reynolds numbers were between 200 and 1000. Most of these experiments are well above the critical Reynolds number at which the flow past a rising sphere loses axial symmetry (Jenny, Dusek & Bouchet 2004; Natarajan & Acrivos 1993). Unlike the glycerin case, where the particle centre remains stationary, in the water experiments we observed the particles precessing around their equilibrium position, which is probably a manifestation of a related instability. The spin rate reported was measured for this precessing particle.

The diamonds in figure 3 show the measured particle angular velocity Ω_p normalized by the cylinder angular velocity ω as a function of Ta. The filled symbols are data taken with the 4 mm radius sphere, while the open symbols refer to the 3.1 mm radius sphere. The difference between the two sets illustrates the effect of the parameter Ga defined in (2.1). These data clearly indicate that there is a broad range of Ta values for which the particle rotates faster than the cylinder, i.e. faster than the undisturbed flow. This is surprising, since, as we have seen in § 1, the known results for streamwise shear would suggest that an increase of inertial effects brings about a decrease in the particle spin rate compared to the ambient rotation. Moreover, to the best of our knowledge, hitherto no such results have been reported.

As the cylinder rotation rate is decreased, the particle equilibrium position moves away from the axis in such a way that Re increases as predicted by (2.4) and (2.5). As shown in figure 3, the normalized particle angular velocity increases as well. To examine the possibility of wall effects, we took data in the same Taylor-number range in the larger cylinder. These data, shown by the triangles in figure 3, are quite consistent with the other ones, which proves that the observed results are not wall effects. The maximum value of Ω_p/ω, about 2.1, is reached for a Reynolds number that can be estimated as 650 ± 100. It should be noted that this is smaller than the

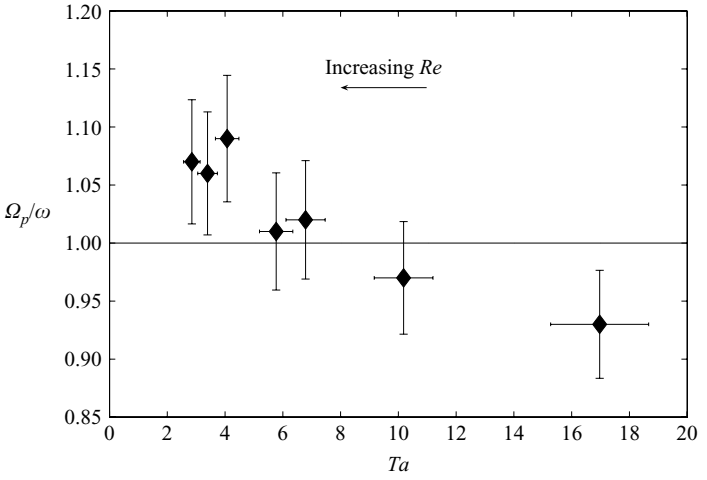

FIGURE 4. Normalized particle spin rate Ω_p/ω versus $Ta = 2\omega R^2/\nu$ for the glycerine–water mixture in the smaller cylinder; the particle radius was 4.0 mm. The corresponding Reynolds number is between 2 and 50, approximately.

Reynolds number for the terminal velocity in still fluid which would be 709 and 1090 for the 3.1 and 4.0 mm spheres, respectively. As the Taylor number is further decreased, Ω_p/ω rapidly falls and the precession of the particle is less regular. It is speculated below in § 9 that these features may have some analogy with the onset of unsteadiness in the case of a sphere rising in a quiescent fluid as the Reynolds number is increased.

When the Taylor number is increased beyond 400 or so, the particle moves closer to the centre, the Reynolds number decreases, and the vorticity parameter Sr_ω increases. Correspondingly, Ω_p/ω falls below 1, reaches a minimum, and then starts rising again toward 1, which is the expected normalized spin rate at very large angular velocities when the particle centre is essentially on the rotation axis.

For the data in figure 3 Sr_ω ranges between about 0.1 and 0.3 to the left of the peak and between about 0.3 and 1 in the descending part of the curve. These values are not very accurate due to the difficulty of getting an accurate reading of r_e, but they do nevertheless demonstrate the trend of the data.

Figure 4 shows the results obtained in the smaller cylinder with the glycerine–water mixture. The resulting Reynolds numbers were an order of magnitude smaller than with water but the effect, although reduced, is still present: as Ta decreases, the particle moves away from the axis and its normalized spin rate increases above 1. This finding suggests that the precessional motion of the sphere observed in water does not qualitatively affect the phenomenon. The diamonds in figure 5 show the same data plotted versus the Reynolds number. As before, a precise measurement of the equilibrium position r_e is difficult and the error bars accordingly rather large; nevertheless, the normalized particle spin rate is greater than 1 at sufficiently low rotation rates. At higher rotation rates the particle moves closer to the axis, the vorticity parameter Sr_ω increases, and Ω_p/ω falls below 1 as before. The fact that this transition from values larger than 1 to values smaller than 1 is observed for very different Reynolds numbers suggests it is mainly dependent on Sr_ω reaching a sufficiently large value, which is comparable in the two cases of water and water–glycerine.

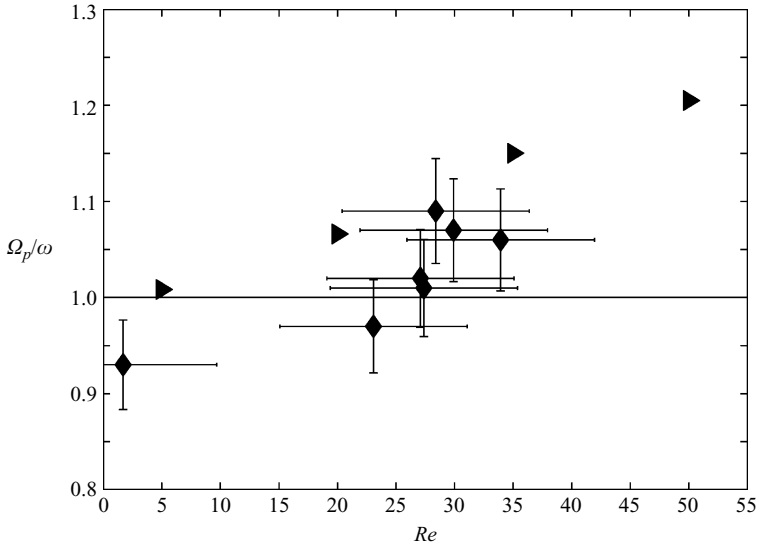

FIGURE 5. The same data for the normalized particle spin rate of figure 4 (diamonds) are plotted versus *Re*. The triangles are numerical results discussed in § 5.

In summary, these experiments conclusively prove that, in a portion of the parameter range (Re, Sr_ω), the normalized angular velocity of a particle increases beyond 1 with distance from the axis, i.e. as the flow velocity seen by the particle, and thus Re, becomes sufficiently large. This trend prevails up to $Re \sim 650$, after which the normalized particle spin rate rapidly decreases. Thus, except when the particle is very close to or very far from the cylinder axis, the particle angular velocity is higher than that of the undisturbed flow.

4. Numerical method

To better understand the behaviour of the particle angular velocity in solid-body rotation compared to simple shearing flow we carried out numerical simulations with different types of flow, described in the next section. In this section we briefly explain our numerical method.

We used the three-dimensional Navier–Stokes solver Physalis (Zhang & Prosperetti 2005). The underlying method rests on the observation that, owing to the no-slip condition, the flow in the immediate neighbourhood of a particle differs at most slightly from a rigid-body motion and can therefore be linearized about such a motion. The resulting set of equations is formally similar to the Stokes equations, for which a general solution (valid only very near the particle) can be written down in terms of an expansion in spherical harmonics with undetermined coefficients (Happel & Brenner 1965; Kim & Karrila 1991). These coefficients are calculated iteratively by matching, in the immediate neighbourhood of the particle, the analytic solution obtained in this fashion to a finite-difference solution. The advantage of this procedure is that it avoids the need to deal with the complex geometry of the actual particle boundary. The finite-difference solution is obtained on a standard Cartesian grid by a second-order projection method. The solution obtained has therefore a dual nature, spectral in a region with a thickness of the order of the mesh size surrounding the particle, and finite-difference further away. Useful features of the technique are that

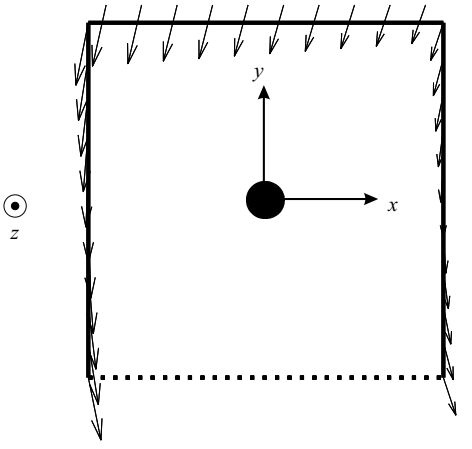

FIGURE 6. Cross-section of the computational domain. The boundaries where Dirichlet boundary conditions are applied are solid, the boundary where von Neumann boundary conditions are applied is dotted.

fewer nodes per particle radius are sufficient for an accurate solution and that the no-slip condition at the particle surface is satisfied exactly. Furthermore, the low-order expansion coefficients are directly proportional to the hydrodynamic force and couple acting on the particle. This property eliminates the need to calculate these quantities by integration of the fluid stress over the particle surface. For details about this method the reader is referred to Zhang & Prosperetti (2005) and for applications to Zhang, Botto & Prosperetti (2006).

For reasons of computational time, most of the simulations were conducted for $Re = 20$ and $Re = 50$, and a few additional ones were carried out for $Re = 5$, 35, 100 and 200. Decreasing the Reynolds number below 5 would require a very large computational domain to avoid boundary effects, while higher Reynolds numbers require a more refined grid. We found that in the Reynolds number range between 5 and 50 it was possible to perform simulations with sufficient domain size and resolution in a reasonable amount of computing time.

The particle centre was placed at the centre of the computational domain which was a cuboid (see figure 6 for a cross-section of the domain). Unless stated otherwise, its dimensions were 20 particle radii in the x- and y-directions and at least 16 in the z-direction, parallel to the axis of rotation. For $Re = 20$, we found that doubling the domain size changed the particle spin rate by no more than 0.4 %, the drag coefficient by about 1 % and the lift coefficient (defined below in (5.1)) by about 3 %. For $Re = 5$ increasing the domain size from 18 to 22 particle radii in each direction changed the drag coefficient by 1.4 %, while the (much smaller) lift coefficient underwent a change of over 30 %. Thus, although the results for $Re = 5$ may have a somewhat lower accuracy, we conclude that our domain size was sufficient for the other cases.

It has been shown in Zhang & Prosperetti (2005) that, for a sphere in uniform flow, 8 nodes per particle radius give an excellent accuracy at $Re = 50$ and an acceptable one even at $Re = 100$. We have used the same number of nodes up to $Re = 50$. To test the resolution, for $Re = 50$ we refined the grid by a factor of 2 in each direction and found that the spin rate and the drag and lift coefficients changed by about 1 % in the case of solid body rotation. For a linear shear flow the absolute differences were comparable but, since in this type of flow the lift coefficient and spin rate are

much smaller, the relative differences were up to 8 % for the particle spin rates and up to 13 % for the lift force, while they remained at the 1 % level for the drag coefficient. Changing the resolution for the cross-stream shear and straining flow yielded differences below the ones of the linear shear flow. For the simulations where $Re > 50$, 16 nodes per particle radius were used.

The accuracy of the spectral representation of the solution in the region near the particle depends on the order N of truncation of the spherical harmonic expansion, i.e. on the number of coefficients retained in the calculation (Zhang & Prosperetti 2005). It was found that $N = 1$, which amounts to retaining only 10 coefficients, yields inaccurate results. For $Re = 50$, truncation at $N = 2$ (25 coefficients) or $N = 3$ (49 coefficients) gave a difference of 2 % in the particle spin rate, 1 % in the lift coefficient, and 0.2 % in the drag coefficient. Therefore, the calculations were done with $N = 2$ and 25 coefficients.

The undisturbed flow velocity was prescribed on all the faces of the computational domain parallel to the rotation axis except the bottom one (figure 6). On the bottom surface the derivative of the horizontal velocity was set equal to the corresponding derivative of the undisturbed velocity (i.e. $-\alpha\omega$, see (6.1)), while the normal derivative of the normal velocity was set to zero. Periodicity conditions were imposed on the bounding planes normal to the rotation axis (z-direction). For the auxiliary pressure variable, the standard von Neumann conditions of the second-order projection method (see for example Brown, Cortez & Minion 2001; Zhang & Prosperetti 2005) were used.

5. Numerical results for solid-body rotation, varying Re

A first set of simulations was conducted for a particle immersed in a liquid in solid-body rotation with prescribed values of Re and Sr_ω. In this case, as in the other simulations described later, the particle centre was kept fixed but the particle was allowed to freely rotate.

Although it would have been desirable to conduct a simulation releasing the particle and allowing it to find its equilibrium position, the huge amount of computational time required prevented us from doing this. Thus, the particle was placed to the left of, and at different distances from, the rotation axis (figure 7*a*), depending on the desired shear rate. In principle, for a given Reynolds number and shear rate, (2.4) can be solved to give a specific value of Ga/Ta, which suggests that the situations we simulate are physically realizable.

The symbols in figure 8 show the drag on the sphere for different Reynolds numbers for both rotating and non-rotating particles. The differences in the drag coefficient are so small that they are not visible here. The solid line is the standard drag curve for uniform flow, which predicts a slightly smaller drag. Numerical values are given in table 1 together with those of other authors and our own for uniform flow.

The results for the normalized spin rate Ω_p/ω vs. the Reynolds number are shown in figures 5 and 9. Some numerical values are given in table 2. All our numerical results indicate that the normalized spin rate Ω_p/ω is above 1 in the case of a fluid in solid-body rotation. Thus the particle spins faster than the surrounding fluid, just as previously seen in experiments. As mentioned before, this behaviour is at variance with that reported in the simulations of Bagchi & Balachandar (2002*b*) who, as indicated in table 2, found a decrease in the normalized spin rate at these Reynolds numbers. For comparison with another flow situation, table 2 also shows results for

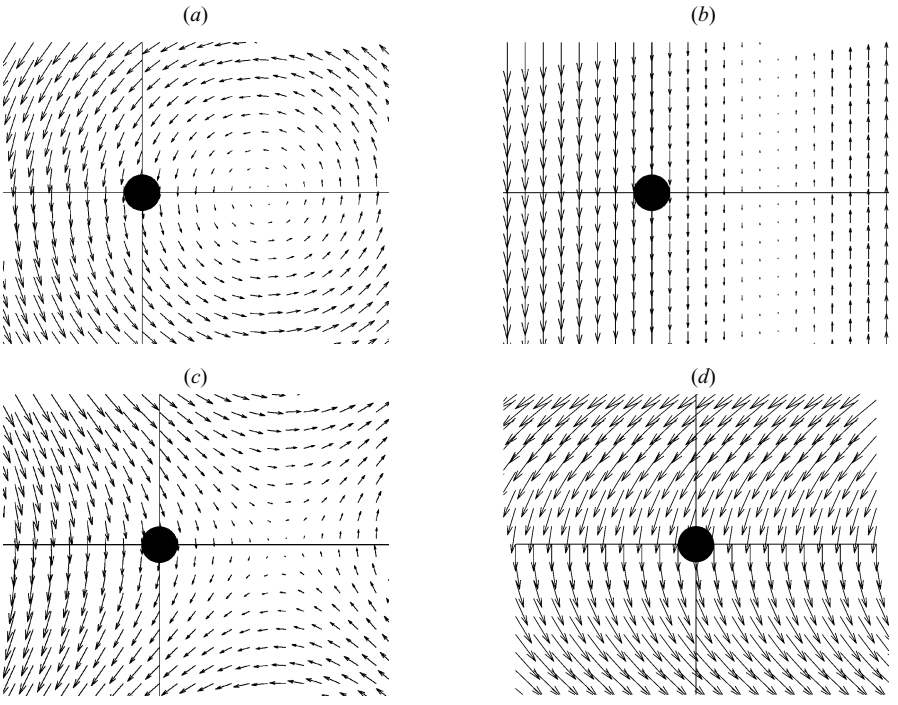

FIGURE 7. Examples of the flow fields of the family of flows (6.1): (*a*) solid-body rotation, $\alpha = 1$, $\beta = 1$; (*b*) linear shear, $\alpha = 0$, $\beta = 1$; (*c*) strain, $\alpha = -1$, $\beta = 1$; (*d*) cross-stream shear, $\alpha = 1$, $\beta = 0$.

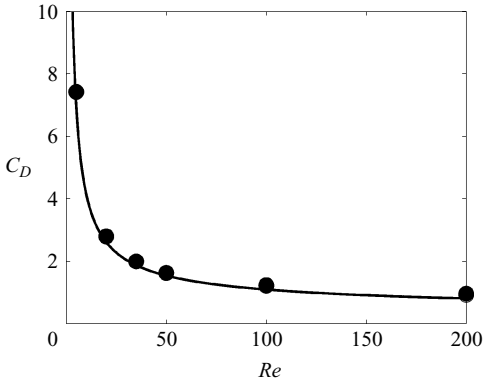

FIGURE 8. Drag coefficient for a particle in solid-body rotation, $Sr_\omega = 0.1$, (symbols) compared with the standard drag curve $C_D = (24/Re)(1 + 0.15Re^{0.687})$ for a uniform flow. The data points for $Re = 100$ and $Re = 200$ were calculated with doubled spatial resolution, but a smaller domain.

a linear shear flow. For this case the results of Bagchi & Balachandar (2002*a*) and our own agree.

The triangles in figure 5 are the normalized spin rates for some of these simulations, all with $Sr_\omega = 0.1$. In this figure the numerical results are compared with some of the experimental results (diamonds). The influence of Sr_ω can be deduced from table 2. If $Sr_\omega \ll 1$, there is little influence of Sr_ω on Ω_p/ω as becomes evident

Drag coefficient	$Re = 5$	$Re = 20$	$Re = 50$
Dennis & Walker (1971), uniform flow	7.21	2.73	
Standard drag curve (Clift, Grace & Weber 1978)	6.98	2.61	1.54
Magnaudet, Rivero & Fabre (1995)	6.92	2.71	
Bagchi (2002)			1.57
Present, uniform flow	7.42	2.77	1.59
Present, non-rotating particle in solid-body rotation, $Sr_\omega = 0.1$		2.79	1.62
Present, rotating particle in solid-body rotation, $Sr_\omega = 0.1$	7.83	2.80	1.63
Present, rotating particle in solid-body rotation, $Sr_\omega = 0.04$			1.59

TABLE 1. Drag coefficient, comparison of present simulations with previous results.

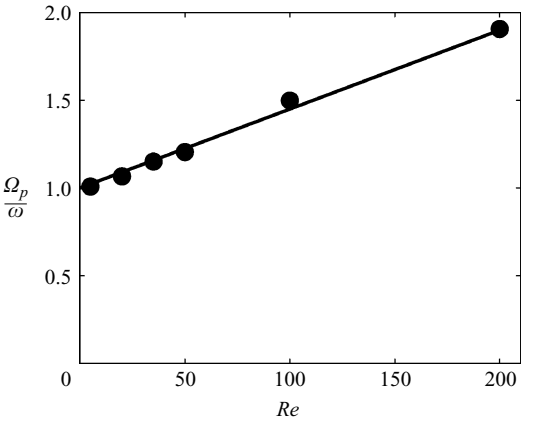

FIGURE 9. Normalized torque-free particle spin rate for a particle in solid-body rotation, $Sr_\omega = 0.1$, as a function of the Reynolds number. The data points for $Re = 100$ and $Re = 200$ were calculated with doubled spatial resolution, but a smaller domain. The solid line is a fit to the data: $\Omega_p/\omega = 1 + 0.0045\ Re$.

Flow type	*Re*	Ω_p/ω, BB	Ω_p/ω, present results
Linear shear	20	0.35 ($Sr = 0.1$)	0.36 ($Sr = 0.05$)
Linear shear	50	0.28 ($Sr = 0.1$)	0.30 ($Sr = 0.05$)
Solid-body rotation	20		1.08 ($Sr_\omega = 1.10^{-4}$), 1.07 ($Sr_\omega = 0.1$)
Solid-body rotation	25	0.85 ($Sr_\omega = 0.04$)	1.10 ($Sr_\omega = 0.04$)
Solid-body rotation	50	0.74 ($Sr_\omega = 0.04$)	1.25 ($Sr_\omega = 0.04$), 1.24 ($Sr_\omega = 0.1$)

TABLE 2. Normalized torque-free particle spin rates, results of Bagchi & Balachandar (BB) compared with the present results.

by comparing simulations at different Sr_ω, but at the same Reynolds number. For example, decreasing Sr_ω by a factor of 1000 at $Re = 20$ has hardly any effect on the ratio Ω_p/ω. This indicates that the ratio Ω_p/ω is much more sensitive to Re than to Sr_ω for $Sr_\omega \ll 1$. However, for high values of Sr_ω the particle position is near the axis, which has a strong effect on Ω_p/ω owing to the resulting strong inhomogeneity of the flow incident on the particle (see also the end of the section). The experimental data

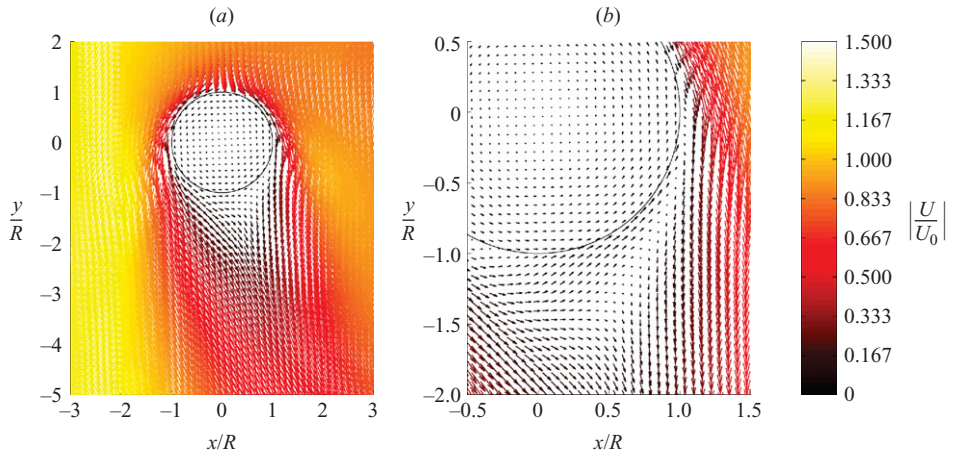

FIGURE 10. Computed velocity field in the symmetry plane for the flow around a sphere immersed in a liquid in solid-body rotation ($\alpha = 1$, $\beta = 1$, $Sr_\omega = 0.1$), $Re = 20$ (a), and a higher-resolution close up (b). The length of the arrows, which are colour-coded, is proportional to the velocity. The flow parameters α and β will be explained in § 6.

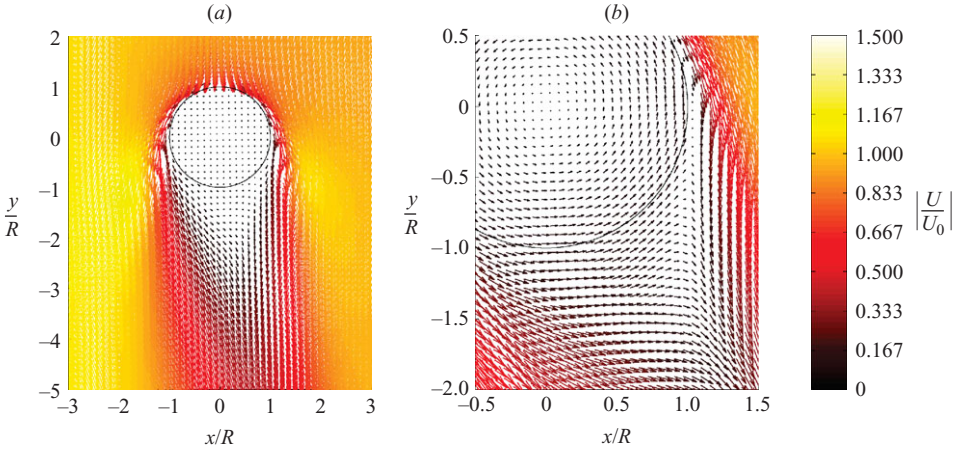

FIGURE 11. As figure 10 but for $Re = 50$.

(diamonds) in figure 5 have in general a much higher shear rate than the numerical simulations, in particular the left-hand data points.

The triangle corresponding to $Re = 5$ in figure 5 shows an angular velocity close to the Stokes limit. The spin rate increases with Re, the behaviour being comparable to that seen in the experimental data in the same figure. Figures 10 and 11 show the velocity field in the symmetry plane in the neighbourhood of the particle for $Re = 20$ and 50, respectively. At the higher Reynolds number (figure 11) the wake extends to a much greater distance behind the particle but is less deflected. Also, velocities in the near-wake region are larger in the latter case.

Auton (1987) expressed the force $\boldsymbol{F}_L$ on a stationary particle immersed in an inviscid rotational flow with undisturbed velocity $\boldsymbol{U}$ at the position of the particle centre in the form

$$\boldsymbol{F}_L = \tfrac{4}{3}\pi R^3 \rho C_L \boldsymbol{U} \times (\nabla \times \boldsymbol{U}), \tag{5.1}$$

Flow type	Re	C_L, BB	C_L, present results
Linear shear, R	20	0.18 ($Sr = 0.1$)	0.19 ($Sr = 0.05$)
Linear shear, NR	20	0.04 ($Sr = 0.1$)	0.05 ($Sr = 0.05$)
Linear shear, R	50	0.11 ($Sr = 0.1$)	0.13 ($Sr = 0.05$)
Solid-body rotation, R	20		0.66 ($Sr_\omega = 10^{-4}$), 0.65 ($Sr_\omega = 0.1$)
Solid-body rotation, NR	20		0.45 ($Sr_\omega = 0.1$)
Solid-body rotation, R	25	4.29 ($Sr_\omega = 0.04$)	0.71 ($Sr_\omega = 0.04$)
Solid-body rotation, NR	25	4.14 ($Sr_\omega = 0.04$)	
Solid-body rotation, R	50	3.05 ($Sr_\omega = 0.04$)	0.90 ($Sr_\omega = 0.04$), 0.86 ($Sr_\omega = 0.1$)
Solid-body rotation, NR	50		0.64 ($Sr_\omega = 0.1$)

TABLE 3. Comparison of the results for the lift coefficient (defined in (5.1)) of Bagchi & Balachandar (BB) and the present results for rotating (R) and non-rotating (NR) spheres.

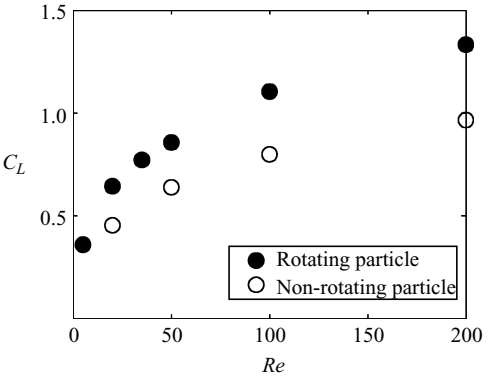

FIGURE 12. Dependence of the calculated lift coefficient defined in (5.1) on the Reynolds number ($Sr_\omega = 0.1$). The data points for $Re = 100$ and $Re = 200$ were calculated with doubled spatial resolution, but a smaller domain.

and calculated the value of the lift coefficient C_L as $1/2$. As expected, owing to viscous effects and particle spin, our results, shown in table 3, differ from this value. The table also shows significant differences between our computations and those of Bagchi & Balachandar (2002*b*) for the present case of solid-body rotation, while the two calculations agree for linear shear.

Not unexpectedly, particle spin is found to have a much greater effect on the lift than on the drag coefficient. For example, for a non-rotating sphere at $Re = 20$, $C_L = 0.45$ and $C_D = 2.79$ while, when the particle is allowed to rotate, C_D increases only slightly to 2.80, while C_L grows by over 40 % to 0.65. These and other numerical values for $Re = 50$ and $Sr_\omega = 0.1$ are given in table 3 and are shown for C_L graphically in figure 12 by the filled (rotating) and open (non-rotating) symbols. In both cases the lift coefficient increases with the Reynolds number. The difference between the rotating and non-rotating cases increases with Re as well. This is in line with the fact that the particle rotates faster at higher Re. The lift coefficient must go to zero as $Re \to 0$ and, the computed result for $Re = 5$ does indeed indicate a strong decrease in C_L.

For Sr_ω of order 1 the normalized particle spin rate drops below 1. For $Sr_\omega = 2$, for which the axis of rotation touches the particle surface, a normalized particle spin rate of 0.93 was found on a domain of 10 particle radii in each direction. This situation

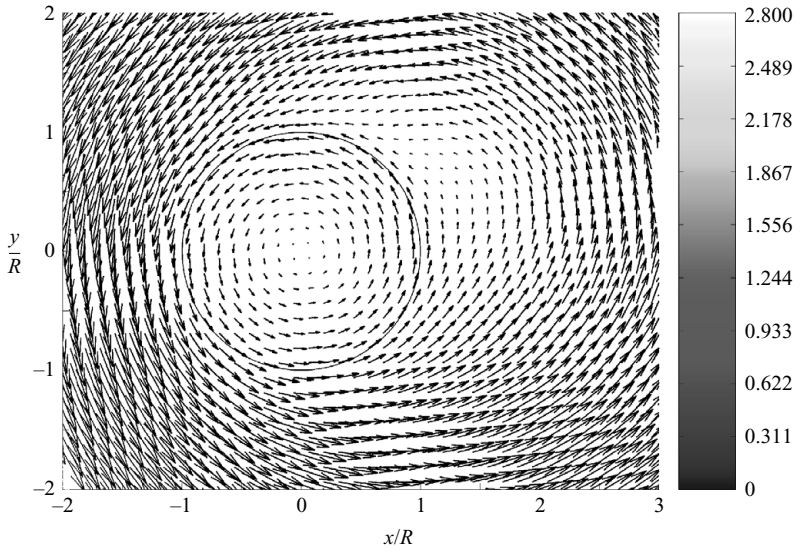

FIGURE 13. Velocity field in the symmetry plane for the flow around a sphere immersed in a liquid in solid-body rotation for a large vorticity parameter case, $Sr_\omega = 2$, $Re = 20$. The axis of rotation is located at $(x/R, y/R) = (1, 0)$ and therefore touches the surface of the sphere.

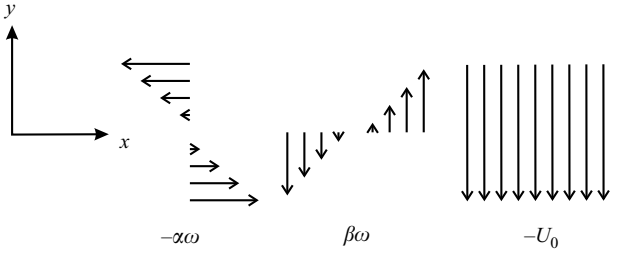

FIGURE 14. The three base flows constituting the family of flows described in § 6 and studied in § 7.

is comparable to that in experiments where the particle finds its equilibrium close to the cylinder centre. Here a low particle spin rate was found too. Figure 13 shows the flow around the particle for this high value of the vorticity parameter Sr_ω. The flow near the axis of rotation, located at $(x/R, y/R) = (1,0)$, is strongly disturbed, with a drastic effect on the incident flow.

6. A family of flows

A solid-body rotation can be considered as the result of adding two two-dimensional shear flows in orthogonal directions (figure 14). As we have seen in § 2, when only a streamwise shear is present, the spin rate of the particle is smaller than that of the fluid, provided inertia is relevant. In contrast, at least in some parameter range, the opposite is true when both shear components are present, as found in our experiments and simulations of particles in rotating flows. To better understand the nature of these differences in behaviour, we consider the following family of flows which smoothly

interpolates between simple shear and solid-body rotation

$$\boldsymbol{U}(x, y) = -\alpha\omega y\hat{\boldsymbol{e}}_x + (\beta\omega x - U_0)\hat{\boldsymbol{e}}_y. \tag{6.1}$$

(For a study of the kinematics of these flows see Kobayashi & Coimbra (2005).) The term $-U_0$ ($U_0 > 0$) represents a uniform flow, while α and β set the magnitude of the cross-stream and streamwise shear components, respectively (figure 14). The vorticity and the shear rate s of this flow field are given by

$$\nabla \times \boldsymbol{U} = \omega(\beta + \alpha)\hat{\boldsymbol{e}}_z, \qquad s = \frac{\partial U_x}{\partial y} + \frac{\partial U_y}{\partial x} = \omega(\beta - \alpha), \tag{6.2}$$

respectively, and both are constants. The vorticity parameter Sr_ω defined in (2.3) then is

$$Sr_\omega = \frac{\omega(\beta + \alpha)R}{U_0}. \tag{6.3}$$

In a straining flow this is not a useful parameter since then $\beta = -\alpha$ and thus $Sr_\omega = 0$. Therefore in addition we introduce the ratio

$$Sr = \frac{sR}{U_0} = \frac{\omega(\beta - \alpha)R}{U_0}, \tag{6.4}$$

which is a dimensionless measure of the shear rate. In the simulations described in the next section the particle Reynolds number is kept fixed while the parameters α and β are varied.

To investigate the effect of shear in the cross-stream direction, the streamwise shear parameter β is set to 1 while the cross-stream shear parameter α is varied between –1 and 1. When $\alpha = 1$, the liquid is in solid-body rotation as in figure 7(*a*). For $\alpha = 0$ the sphere is in a streamwise shearing flow, with the shear in the same direction as the uniform component, see figure 7(*b*). For $\alpha = -1$ the flow is a combination of a pure straining and a uniform downward flow, with the particle displaced horizontally from the centre of strain, as in figure 7(*c*). Intermediate values of α interpolate between these situations.

To see the influence of streamwise shear, when a cross-stream shear component is also present, the parameter α is set to 1 and the parameter β is varied between –1 and 1. For $\beta = 1$ we have the same solid-body rotation as in figure 7(*a*). For $\beta = 0$ we have a uniform flow with a cross-stream shear. The local incident flow field around the particle is shown in figure 7(*d*). For $\beta = -1$ once again we find a combination of a uniform component and a strain, except that now the strain is in the direction opposite to that shown in figure 7(*c*).

7. Numerical results for fixed Re, varying α and β

At steady state, a particle immersed in the flows described in the previous section will rotate with an angular velocity Ω_p such that the hydrodynamic couple to which it is subject vanishes. In the Stokes limit the angular velocity of the particle will be the same as that of the fluid so that $\Omega_p/\omega = \frac{1}{2}(\beta + \alpha)$.

In figure 15 the particle angular velocity, normalized by ω, is shown as a function of the parameter α, with β fixed to 1, or β, with α fixed to 1. If α or β is set to 1, while the other parameter is varied, in the Stokes limit the result is independent of which parameter is held fixed and which one is varied, as indicated by the dotted line in the figure: the angular velocity of the particle increases linearly with both α and β, and therefore also with the vorticity. When inertial effects are accounted for,

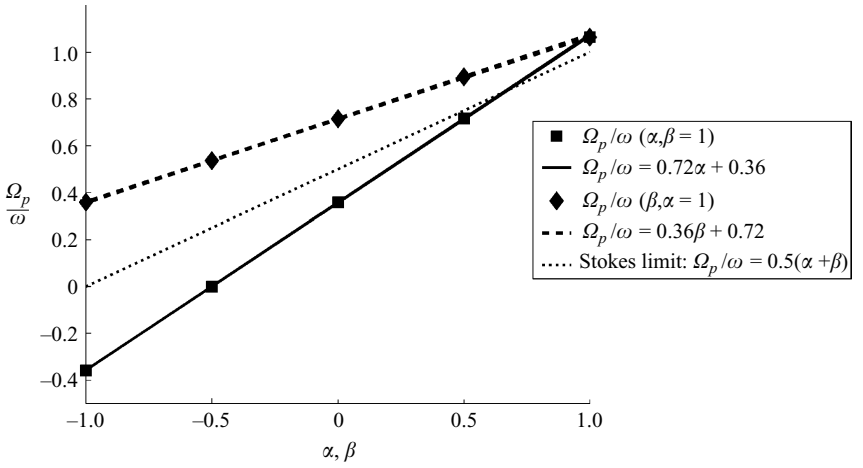

FIGURE 15. Particle angular velocity normalized by ω vs. α, for $\beta = 1$ (squares), and β, for $\alpha = 1$ (diamonds) for $Re = 20$; the dotted line is the Stokes result. The solid and dashed lines show the result obtained by linearly superposing the values of Ω_p/ω induced separately by each shear flow type.

however, it is relevant which of the two shear components is varied. For the results shown in figure 15 the Reynolds number is 20. When the streamwise shear is fixed ($\beta = 1$, squares), the spin rate is below the Stokes value over most of the range except when the cross-stream component is close to 1. When the cross-stream component is fixed, however ($\alpha = 1$, diamonds), the spin rate is always above the Stokes value. These results clearly show that the angular velocity of the particle more strongly depends on the cross-stream than on the streamwise shear.

The case $\alpha = 0$, $\beta = 1$ (middle square in figure 15) represents a linear shear flow, the shear component being in the flow direction. We find $\Omega_p/\omega = 0.36$, the decrease with respect to the Stokes limit ($\Omega_p/\omega = 0.5$) being due to inertial effects. The flow field in the symmetry plane can be seen in figure 24(b). For the same Reynolds number, the fit (1.7) to Bagchi & Balachandar's (2002a) results predicts a normalized particle angular velocity of $\Omega_p/\omega = 0.35$, very close to our value (see table 2).

In the pure strain cases ($\alpha = 1$, $\beta = -1$ or $\alpha = -1$, $\beta = 1$) the particle is found to rotate with $\Omega_p/\omega = 0.36$ and –0.36, respectively, in spite of the fact that the undisturbed flow itself has no vorticity. Bagchi & Balachandar (2003) considered the case of a particle moving through a straining field and also found the particle to rotate as long as neither of the principal axes of the strain was aligned with the relative velocity. This case is quite similar to our situation of a particle fixed in a straining flow to which a uniform flow is added, and indeed in our case no principal axis of the strain is aligned with the uniform flow component. The streamwise shear induces a clockwise rotation, whereas the cross-stream shear induces a counterclockwise rotation when $\alpha = 1$, $\beta = -1$. The contribution of the streamwise shear component appears to be less effective, so that the resultant spin is in the direction of the cross-stream shear. The cross-section of the flow field around the particle shown in figure 24(e) indicates a deflection of the wake to the right due to the cross-stream shear. For a cross-stream shear with $\alpha = 1$, $\beta = 0$ (middle diamond in figure 15), we find $\Omega_p/\omega = 0.72$, which is an increase with respect to the Stokes limit ($\Omega_p/\omega = 0.5$).

To better understand these different phenomena, the effects of the two shear types were investigated separately by setting one of the parameters to 0 and varying the

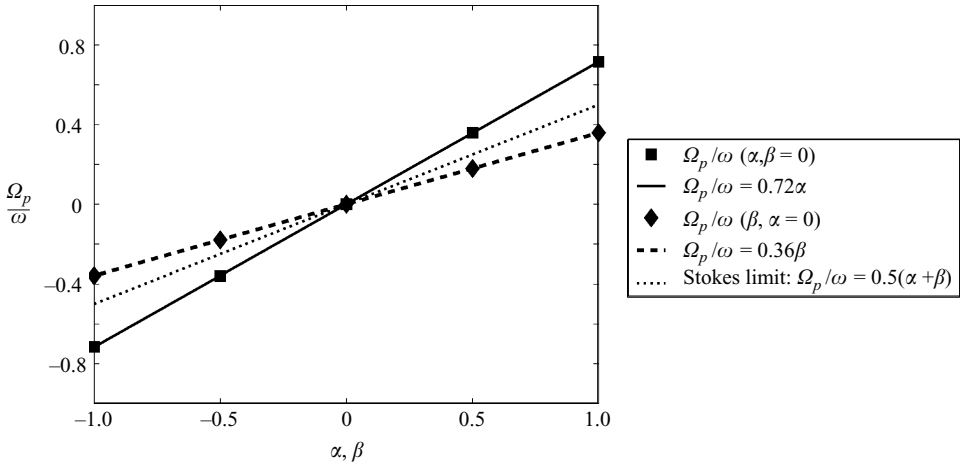

FIGURE 16. Particle angular velocity normalized by ω vs. α, for $\beta = 0$ (squares) and β, for $\alpha = 0$ (diamonds) for $Re = 20$; the dotted line is the Stokes result. The solid and dashed lines represent linear fits.

Flow type	α	β	Ω_P/ω	α	β	Ω_P/ω	α	β	Ω_P/ω
	$Re \to 0$			$Re = 20$			$Re = 50$		
Linear shear	0	1	0.5	0	1	0.36	0	1	0.30
Cross-stream	1	0	0.5	1	0	0.72	1	0	0.91
Solid-body rotation	1	1	1	1	1	1.07	1	1	1.20
Strain	1	−1	0	1	−1	0.36	−1	1	−0.61

TABLE 4. Results for the normalized particle angular velocity for different types of flow at $Re = 20$ and $Re = 50$ compared with the results for Stokes flow.

other one. The results are shown in figure 16; as before, the dotted line is the Stokes limit. Once again, the cross-stream shear gives rise to a much higher spin rate (in modulus) than the streamwise shear. The results of the cross-stream shear lie above the Stokes limit, those of the streamwise shear below. So, whereas inertial effects decrease the particle spin rate due to streamwise shear, they increase it in the presence of a cross-stream shear.

In figure 15, the solid line closely matching the squares shows the relation $\Omega_p/\omega = 0.36 + 0.72\,\alpha$ and is the sum of 0.36, the normalized angular velocity calculated for $\alpha = 0$ and $\beta = 1$ (streamwise shear flow), and a linear fit to the value of Ω_p/ω calculated for $\beta = 0$ and variable α (i.e. variable cross-stream shear, see figure 16). Similarly, the dashed line represents the relation $\Omega_p/\omega = 0.72 + 0.36\,\beta$, which is the sum of the angular velocity calculated for $\alpha = 1$ and $\beta = 0$ (cross-stream shear flow), 0.72, and a linear fit to the value of Ω_p/ω calculated for $\alpha = 0$ and variable β. In table 4 the torque-free particle spin rates for different flow types at different Reynolds numbers are given. Apparently, one can add, resp. subtract, the particle spin rates in a cross-stream shear and a streamwise shear to find the spin rates in a solid-body rotation, resp. straining flow. It is remarkable that a linear combination very accurately reproduces the computational results in spite of the nonlinearity of the governing equations. Probably this is a consequence of the relative smallness of the shear flows with respect to the incident uniform flow in the cases studied (Sr and

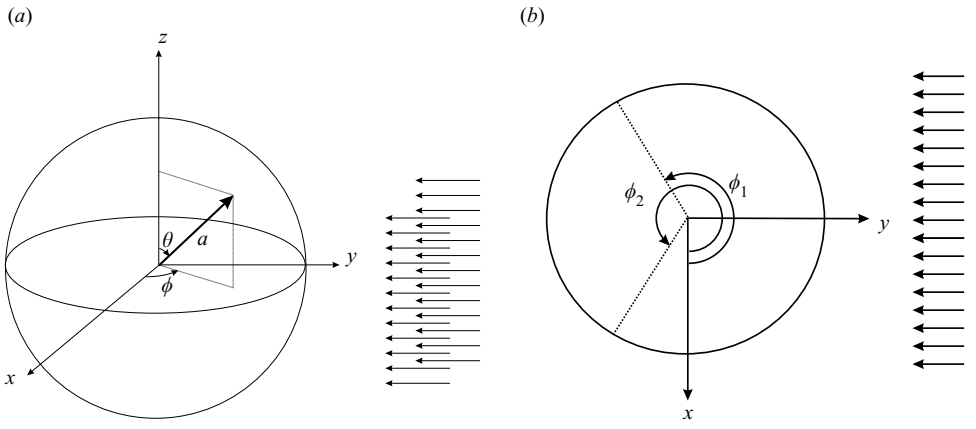

FIGURE 17. (*a*) Coordinate system for the sphere with incoming flow, (*b*) top view of the sphere with the angles ϕ_1 and ϕ_2 marking the region of low shear stress, $|\sigma_{r\phi}/(\mu U_0/a)| < 0.05$.

Sr_ω are of the order 0.1). This finding may be useful as it permits the deduction of properties of the combined flow from those of its individual components.

8. Shear stress

The results of the previous section show a clear distinction between the effects of the streamwise shear flow and the other types of flow on particle spin. The streamwise shear flow causes a decrease in particle spin rate with increasing Reynolds number, whereas all others show an increase (table 4). The increase is smallest for a solid-body rotation, larger for the cross-stream shear and largest for straining flow.

With the coordinates as given in figure 17, the component of the hydrodynamic couple around the rotation axis is

$$T = a^3 \int \sigma_{r\phi} \ (\sin\theta)^2 \, \mathrm{d}\theta \, \mathrm{d}\phi \tag{8.1}$$

in which $a \sin\theta$ is the distance of the surface element $a^2 \sin\theta \ \mathrm{d}\theta \, \mathrm{d}\phi$ from the axis and $\sigma_{r\phi}$ the appropriate component of the viscous stress. The flow around particles prevented from rotating results in a non-zero value for this integral, while it will vanish for particles rotating in a torque-free state. It is therefore interesting to contrast the detailed distribution of $\sigma_{r\phi}$ on the particle surface in these two situations and for the different flows. (A useful feature of the Physalis method is that the values of the shear stress are proportional to the coefficients of the spherical harmonic expansion mentioned in § 5.)

A steady two-dimensional boundary layer separates from a fixed wall at a point of zero shear stress. In our case the boundary layer is three-dimensional and, with a freely rotating particle, on a moving boundary. Thus the situation is much more complex (Délery 2001; Surana, Grunberg & Haller 2006; Williams III 1977; Van Dommelen & Cowley 1990; Degani, Walker & Smith 1998; Dandy & Dwyer 1990). Still, the separated flow behind the sphere will correspond to a region of low $\sigma_{r\phi}$. With reference to figure 17(*b*), we define angles ϕ_1 and ϕ_2 as limiting angles of the low-shear-stress region where $|\sigma_{r\phi}/(\mu U_0/a)| < 0.05$ on the sphere equator. The

coordinate system is shown in figure 17(*a*); the incident flow is in the negative *y*-direction.

Figure 18(*a–c*) displays $\sigma_{r\phi}$ on the sphere for a uniform flow with $Re = 50$. Figure 18(*b*) is a top view of the sphere; figure 18(*a*) shows contours of $\sigma_{r\phi}$ in a $(\phi\,\theta)$-plot. Another way to present this information is a Hammer–Aitoff projection (e.g. Bugayevskiy & Snyder 1995), which has the advantage of preserving areas. Figure 18(*c*) shows this Hammer–Aitoff projection for the uniform flow at $Re = 50$; the contours in panels (*a*), (*c*), and (*d*) are in steps of 0.05. The incoming flow arrives at the sphere along the line $\phi = \pi/2$ where $\sigma_{r\phi} = 0$. Behind the sphere (ϕ between π and 2π), the flow separates, and here we see a large region of low shear stress, the green area.

Figure 18(*d*) shows $\sigma_{r\phi}$ for $Re = 20$. The region of low shear stress (green area) is smaller, indicating that the flow separates later than for $Re = 50$. Furthermore the values of $\sigma_{r\phi}$ are larger.

We now consider the situation where a solid-body rotation (in the positive *z*-direction, $\alpha = \beta = 1$ in (6.1)) is added to the uniform flow. Figures 19(*e*) and 19(*f*), respectively for a non-spinning and a spinning sphere, permit a comparison of the stress distribution in the two cases. It can be seen that the region of low shear stress (the white region) is shifted somewhat clockwise for the spinning particle (figure 19*f*) compared to the non-spinning one (figure 19*e*). Both ϕ_1 and ϕ_2 decrease (compare the location of the contours near the dotted $5\pi/4$ and $7\pi/4$ lines), suggesting that the flow remains attached longer on the side of positive x (as defined in figure 17) and detaches at an earlier stage for negative x. Close examination of figures 19(*e*) and 19(*f*) shows that the front stagnation point moves a little counterclockwise for a spinning sphere.

In figures 18(*e*) and 18(*f*) the uniform-flow distribution is subtracted from the solid-body rotation at $Re = 20$. The less positive values of $\sigma_{r\phi} - \sigma_{r\phi,\,uniform}$ close to the dotted $5\pi/4$ and $7\pi/4$ lines suggest that the flow separates at lower ϕ-values for the spinning particle. Furthermore the front stagnation point shifts counterclockwise as before owing to the particle spin.

The plots at the left of figure 19 display the $(r\phi)$-component of the shear stress for a non-rotating particle in the four cases of streamwise shear, cross-stream shear, solid body rotation and strain. The region of low shear stress is the white region. The angle ϕ_1 shifts to higher values in the sequence streamwise shear, solid-body rotation, cross-stream shear, strain. Note that this is the same order as found for the Reynolds number dependence of the particle spin. There is also a small shift in ϕ_2. A larger value of ϕ_1 indicates that the shear stress remains high along a larger fraction of the sphere surface on the positive shear stress side, which helps the particle spin. A larger ϕ_2, on the other hand, suggests an earlier separation on the side of the negative shear stress. This means that a shift of ϕ_1 and ϕ_2 in the direction of rotation favours the particle spin. When the particle is rotating as shown in the right panels of figure 19, the differences between the flow types become less clear, since the particle spin causes the region of low shear stress to move back. For example, the particle in a solid-body rotation spins faster than in a streamwise shear. As a result, the region of low shear shifts clockwise and ends up at almost the same location as for the streamwise shear.

In figure 20 the uniform flow result is subtracted from the other flow types for $Re = 20$. In the a-plots we can see that the shear stress distribution remains quite symmetric for a streamwise shear, as is also clear from the top view in figure 18(*g*).

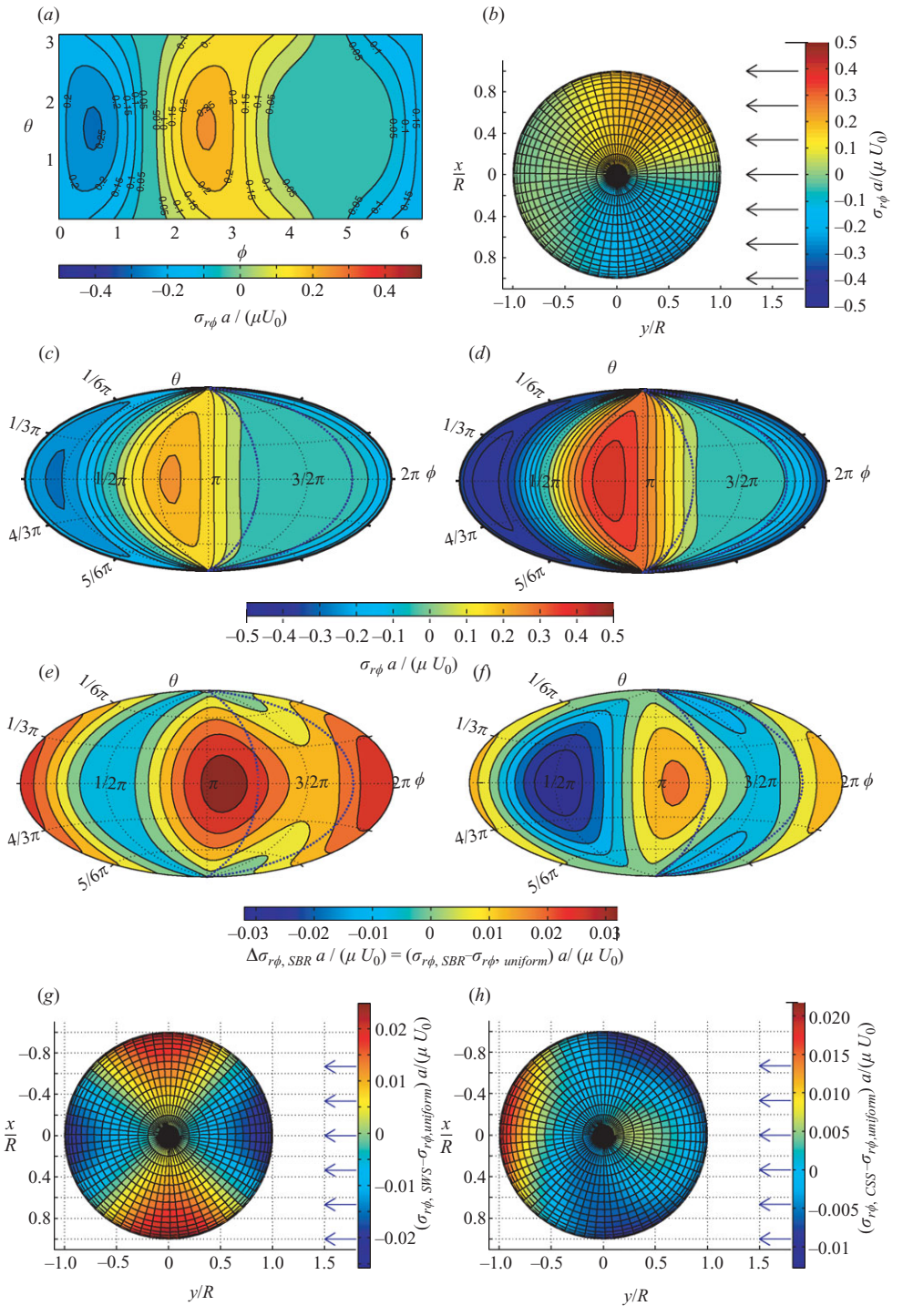

FIGURE 18. $\sigma_{r\phi}$. (*a*) Uniform flow, $Re = 50$, $(\phi\,\theta)$-plot, (*b*) top view or xy-projection, (*c*) Hammer–Aitoff projection. (*d*) Uniform flow, $Re = 20$, Hammer–Aitoff projection. (*e*) Difference between solid-body rotation and uniform flow, $Re = 20$, non-rotating, (*f*) as (*e*) but, rotating. (*g*) Top view of difference between streamwise shear and uniform flow, $Re = 20$, rotating. (*h*) Top view of difference between cross-stream shear and uniform flow, $Re = 20$, rotating. For the definition of ϕ and θ, see figure 17.

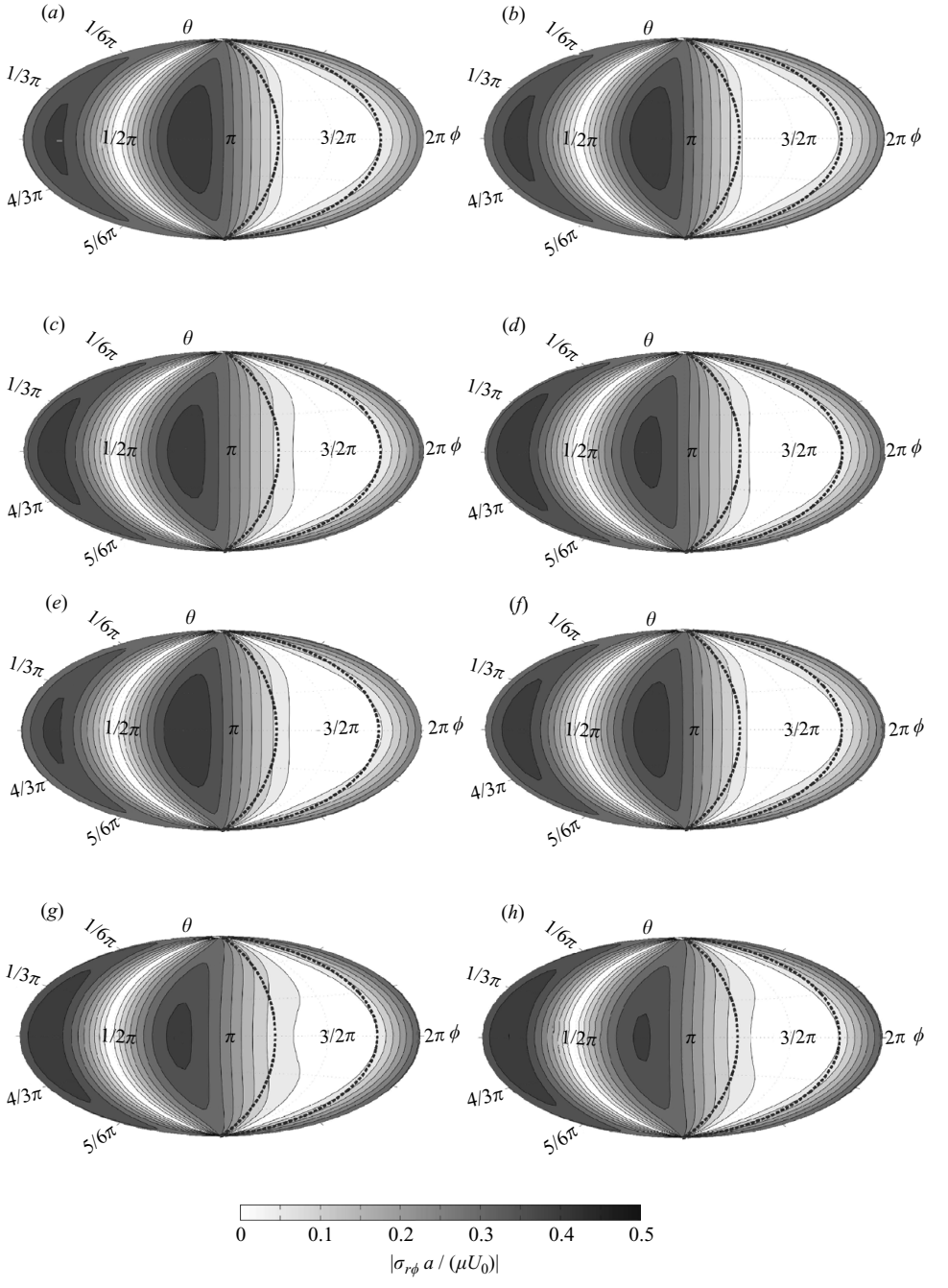

FIGURE 19. $|\sigma_{r\phi}|$, $Re = 20$. (*a*) Streamwise shear ($Sr = 0.05$, $Sr_\omega = 0.05$), non-rotating, (*b*) rotating. (*c*) Cross-stream shear ($Sr = 0.05$, $Sr_\omega = 0.05$), non-rotating, (*d*) rotating. (*e*) solid-body rotation ($Sr = 0$, $Sr_\omega = 0.1$), non-rotating, (*f*) rotating. (*g*) Strain ($Sr = 0.1$, $Sr_\omega = 0$), non-rotating, (*h*) rotating. For the definition of ϕ and θ, see figure 17.

If we add ($\sigma_{r\phi,\,sws} - \sigma_{r\phi,\,uniform}$ for a streamwise shear, figure 20*a*) and ($\sigma_{r\phi,\,css} - \sigma_{r\phi,\,uniform}$ for the cross-stream shear, figure 20*b*), we obtain the result indicated in

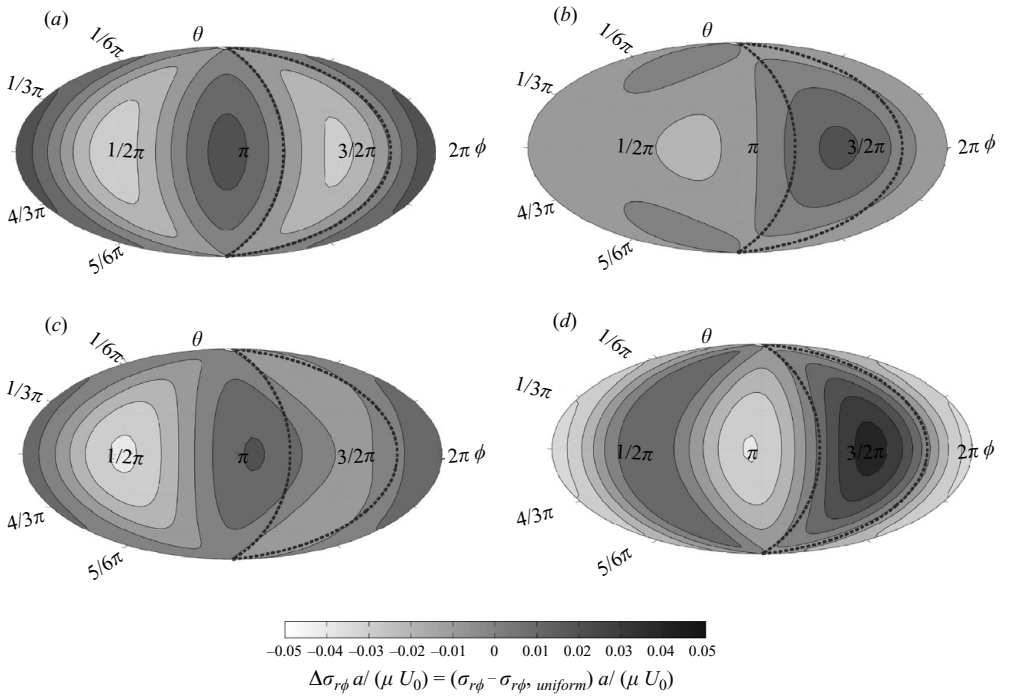

FIGURE 20. Differences in $\sigma_{r\phi}$ with uniform flow, $Re = 20$, rotating particle: (*a*) streamwise shear shear, (*b*) cross-stream shear, (*c*) solid-body rotation, (*d*) strain. For the definition of ϕ and θ, see figure 17.

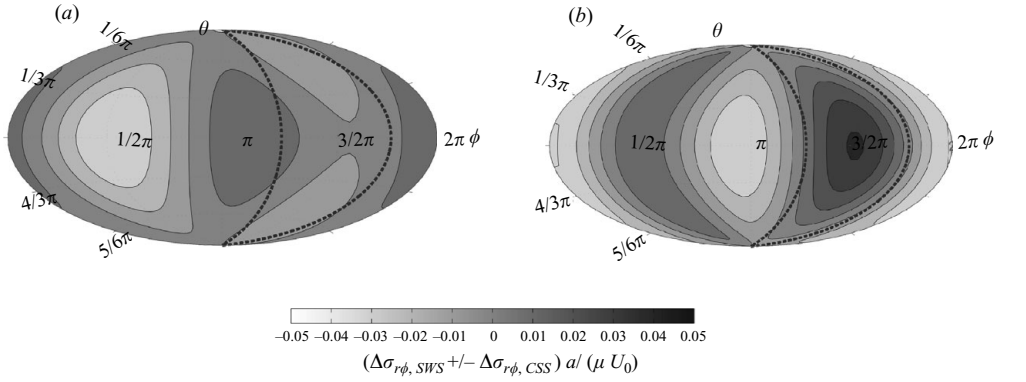

FIGURE 21. Differences in $\sigma_{r\phi}$ of a streamwise and a cross-stream shear: (*a*) added, (*b*) subtracted. $Re = 20$. For the definition of ϕ and θ, see figure 17.

figure 21(*a*), with a striking resemblance with figure 20(*c*). Upon subtracting the two quantities (figure 21*b*) we find a result very close to that of figure 20*d* for the straining flow. Thus, we can simply add, or subtract, the excess $\sigma_{r\phi}$ with respect to uniform flow for streamwise and cross-stream shear to find approximately the result for solid body rotating or straining flow. For $Re = 50$ this approximation is still good (figures 22 and 23). We found earlier in § 7 the same additive property for the particle spin rates.

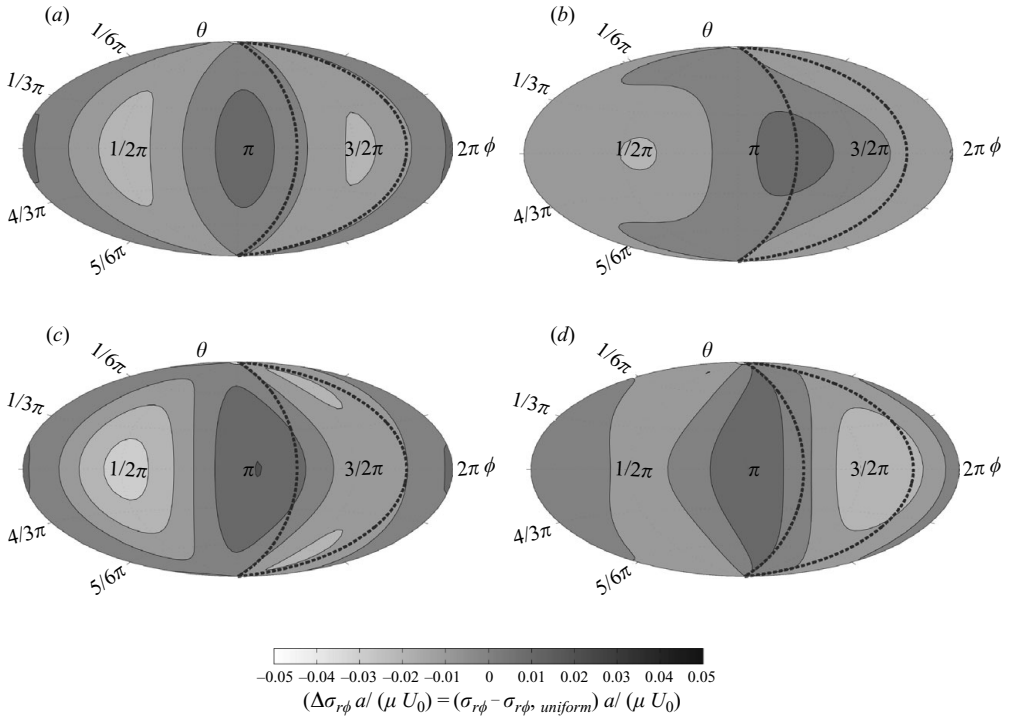

FIGURE 22. Differences in $\sigma_{r\phi}$ with uniform flow, $Re = 50$, rotating particle: (*a*) stream-wise shear shear, (*b*) cross-stream shear, (*c*) solid-body rotation, (*d*) strain. For the definition of ϕ and θ, see figure 17.

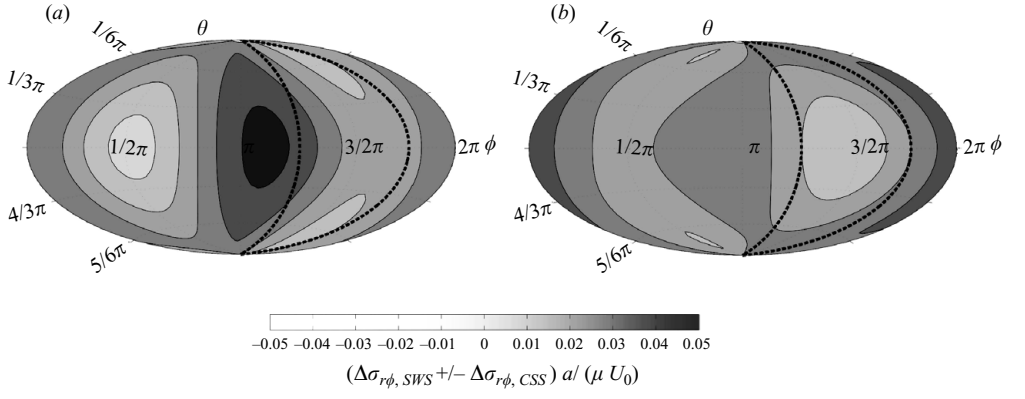

FIGURE 23. Differences in $\sigma_{r\phi}$ of a streamwise and a cross-stream shear: (*a*) added, (*b*) subtracted. $Re = 50$. For the definition of ϕ and θ, see figure 17.

9. Physical considerations

In § 7 we have seen that a linear addition for the spin rates is possible for $Re = 20$ and $Re = 50$. The results in § 8 show that the same holds for the change in the $(r\phi)$-component of the shear stress due to a disturbance of the uniform flow. Furthermore, when adding a shear component to the uniform flow, a shift of the low-shear region was seen. What causes the displacement?

For a fixed, non-rotating particle the previous expression (8.1) for the torque may be written as

$$T = -\mu a^3 \int \omega_\theta \sin^2\theta \, \mathrm{d}\theta \, \mathrm{d}\phi. \tag{9.1}$$

When a sphere is held fixed in a steady uniform flow, an axisymmetric stationary toroidal vortex forms behind it up to a Reynolds number of about 210 (Taneda 1978; Natarajan & Acrivos 1993; Johnson & Patel 1999). In a uniform flow the torque is zero because of the symmetry in ω_θ. Consider now a perturbation of the incident uniform flow in the form of a strain field such as the one shown in figure 7(*c*). This flow, by itself, has no vorticity. Since, as we have seen, the particle rotates in this situation, a non-zero hydrodynamic couple must exist if the particle is prevented from rotating. Since the perturbation carries no vorticity, the hydrodynamic couple must be due to the distortion of the unperturbed vorticity. The strain alters the symmetry of the ω_θ distribution on the particle surface.

It is instructive to consider in this light the different flow situations studied in the previous sections. The left-hand column in figure 24 shows a sketch of the flow type and the right-hand column is the velocity field in the symmetry plane of the sphere perpendicular to the axis of rotation. The sketches in the central column give a qualitative illustration of how the toroidal vortex behind a sphere in steady uniform flow (shown at the top) may be expected to be modified by the addition of various disturbances to the base uniform flow.

The central sketch in figure 24(*b*) shows the modification of the toroidal vortex due to a streamwise shear flow component. The vortex is tilted by the flow. The effect of this on the shift of the wake is not clearly visible in the figure. The effect of a cross-stream shear is much larger. As sketched in figure 24(*c–e*), a cross-stream shear flow tends to displace the toroidal vortex sideways instead of merely tilting it (which is the result of a streamwise shear). The pictures in the right-hand column show that, accordingly, the wake is bent much more strongly. When the cross-stream shear is combined with the streamwise shear to result in a solid-body rotation (figure 24*d*), the two effects sketched separately in figures 24(*b*) and 24(*c*) act together and result in the spin rate for a particle in solid body rotation. Since, with increasing *Re*, the strength of the toroidal vortex increases, it is reasonable to conclude that the magnitude of the spin will also increase, as indeed found up to a maximum Reynolds number in the data shown in figure 3. In the pure straining flow case of figure 24(*e*), the streamwise shear opposes the particle spin induced by the cross-stream shear, but the sideways displacement of the vortex ring is more powerful and the particle still spins, though with a lower angular velocity.

The results of figures 15 and 16 show that shear flow in the cross-stream direction increases the particle spin much more than streamwise shear flow. Harper & Chang (1968) investigated a particle moving through a shear field in an arbitrary direction. In their case as well one can see from their lift coefficient that the cross-stream shear has a stronger effect than a streamwise one. This seems to be a general feature of the type of flows investigated in the present parameter range.

Apart from displacing the wake, the shift of the vortices will change the location of the region of low shear, so instead of looking at the wake displacement, we may also look at the angles ϕ_1 and ϕ_2 discussed in § 8 to obtain an idea of this shift. Here one should remember that there are two competing effects for a rotating sphere: the shear components shift the angles ϕ_1 and ϕ_2 counterclockwise (compare figure 19*a*, *c*, *e*, *g* with 18*d*), while the particle spin shifts them in clockwise

direction (compare figures 19a, c, e, g with b, d, f, h). From studying the non-rotating cases, we know that the shears increase the angles ϕ_1 and ϕ_2 (though the increase in the latter is minor compared to the increase in the former). This implies a shift of the left stagnation point downward and the right stagnation point slightly upwards in figure 24. For the rotating cases the angles are shifted back a little, but in general ϕ_1 is increased. This suggests that the flow remains attached along a larger region on the left-hand side of the sphere than on the right-hand side of the sphere.

So by what mechanism is the particle spin rate decreased for a linear shear and increased for the other flow types? Consider a particle in a uniform flow with its distribution of surface shear, figure 18(d). The torque on the particle is zero. Addition of a linear shear, always keeping the particle from rotating, causes a change in this distribution of surface stress, figure 19(a), but the shift of the low-shear-stress region is not large. There is now a torque on the particle which must be externally opposed in order to prevent particle spin. If we take this torque away, only a relatively small spinning rate is sufficient to relax the torque on the particle to zero. When cross-stream shear, strain or solid-body rotation are added to the uniform velocity, there is a much larger displacement of the low-shear-stress regions, see the large shift in ϕ_1 in figure 19(c, e, g). The reason for this larger shift in ϕ_1 lies in the sideways displacement of the toroidal vortex, due to the cross-stream shear component. A larger spinning rate of the sphere is now needed to relax the torque on the particle to zero.

As the Reynolds number rises, the strength of the vortices will increase. However, owing to stronger convective effects the wake is less deflected. The two competing effects on the wake (increased vortex strength and diminished wake deflection) are reflected in the shear stress values. As the Reynolds number increases, the absolute value of the shear stress decreases (compare figures 18c and 18d). The differences with uniform flow remain, however, comparable for $Re = 20$ and $Re = 50$ (figures 20 and 22). Relatively, the difference with uniform flow is larger for higher Reynolds number. So even though the shear stress decreases for higher Reynolds number, the effective difference with uniform flow increases and the flow effects on the spin rate will increase with the Reynolds number.

What happens in the highest Reynolds number range investigated in the present experiments with water? Uniform flow past a sphere has been studied extensively and exhibits a complex behaviour. The linear stability analysis of Natarajan & Acrivos (1993) reveals a first regular bifurcation to a steady non-axisymmetric flow at $Re \simeq 210$, followed by a Hopf bifurcation at $Re \simeq 270$. These results have been confirmed by Ghidersa & Dusek (2000) and Thompson, Leweke & Provansal (2001). The computations of Johnson & Patel (1999) accounting for a finite deviation from axisymmetric flow confirm the steadiness of a non-axisymmetric regime below $Re \simeq 270$, where they find a transition to organized periodic vortex shedding, a result also found by Tomboulides & Orszag (2000). It is interesting to note that the results of Johnson & Patel (1999) clearly show the presence of a strong toroidal vortex structure behind the sphere even beyond transition to the unsteady regime after the second bifurcation. Computations by Lee (2000) and Lee & Wilczak (2000) also suggest that a non-axially-symmetric vortex structure persists up to a Re in the range 350 to 400, while the flow becomes unsteady for $Re > 400$. On the basis of experimental evidence, Taneda (1978) states that a similar structure, possibly oscillating, persists until $Re \simeq 400$. He reports a major transition for Re between 400 and 1000 where the more-or-less persistent vortex structure behind the sphere is replaced by unsteady

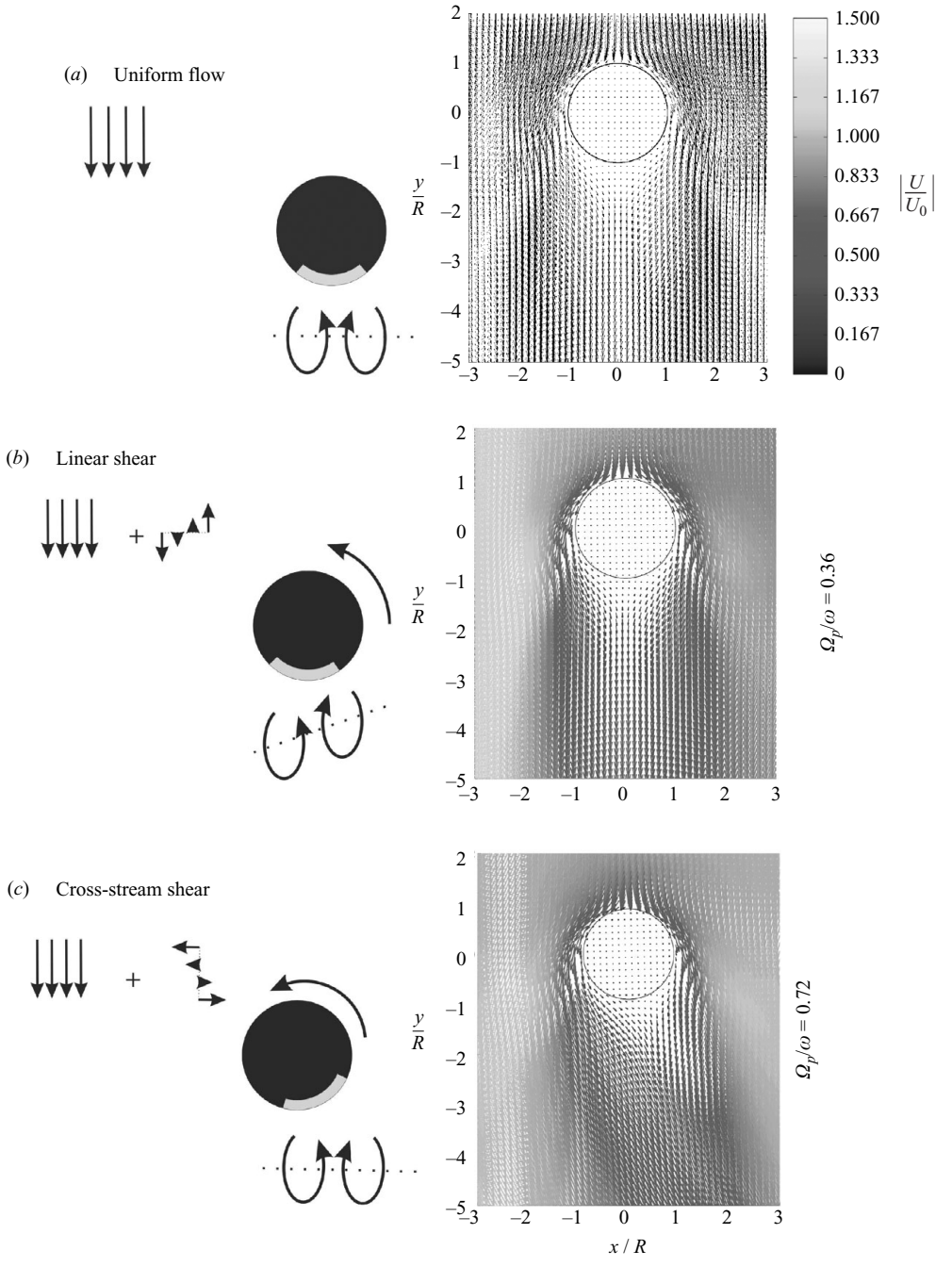

FIGURE 24. (*a–c*) For caption see facing page.

horseshoe-shaped vortex loops. According to Tomboulides & Orszag (2000), a chaotic regime sets in for $Re \simeq 500$. The details of some of these conclusions must be modified in the case of free spheres (Jenny *et al.* 2003, 2004), but the general picture of a first regular bifurcation, followed by a Hopf one, a markedly unsteady and eventually a chaotic regime remains essentially unchanged.

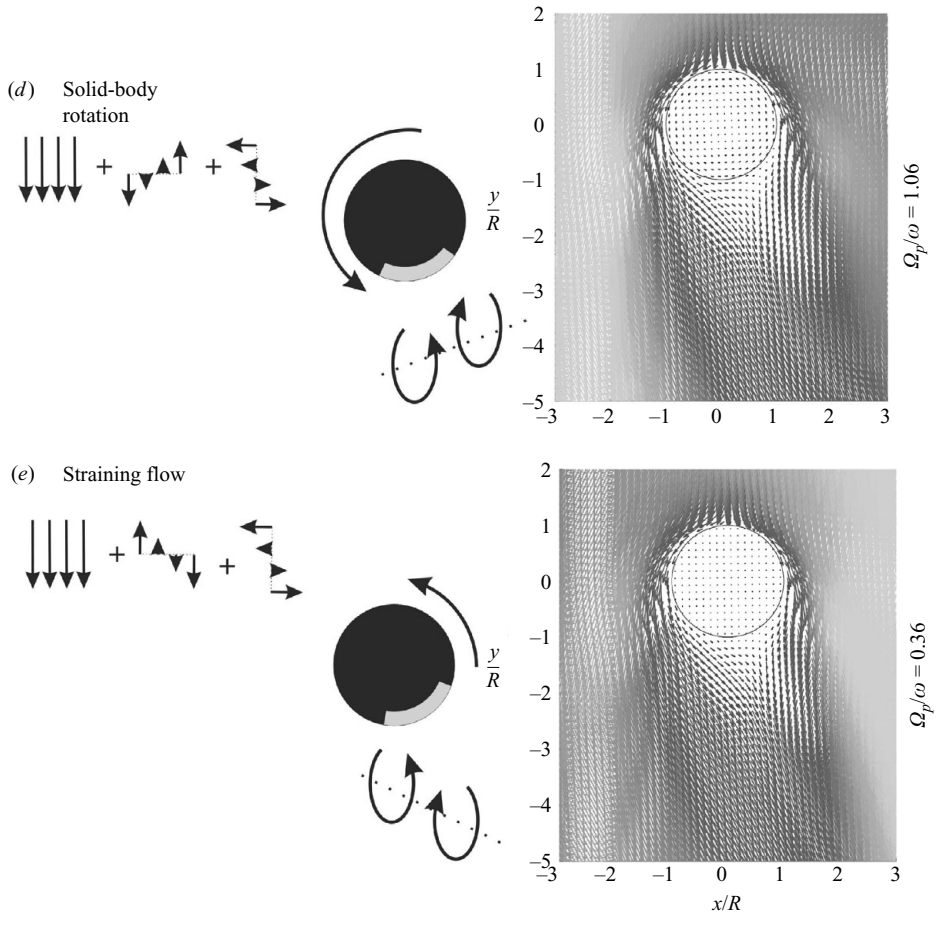

FIGURE 24. Illustration of the proposed mechanism underlying the effects described in this work. The left-hand column shows the components of the flow in which the sphere is immersed. The middle column is a sketch of the displacement of the toroidal vortex and the low-shear-stress region behind the sphere due to the shear components of the flow. The right column shows the calculated velocity field in the symmetry plane of the sphere in the corresponding flow, all for $Re = 20$. (*a*) Uniform flow, $\alpha = 0$, $\beta = 0$; (*b*) linear shear flow, $\alpha = 0$, $\beta = 1$; (*c*) cross-stream shear flow, $\alpha = 1$, $\beta = 0$; (*d*) solid-body rotation, $\alpha = 1$, $\beta = 1$; (*e*) pure strain, $\alpha = 1$, $\beta = -1$.

There does not appear to be any information on how these features are modified in a rotating flow, but for a linear shear flow the results of Lee & Wilczak (2000) show that the same features exist, although the onset threshold is lowered. It may be reasonable to expect that, in our case, the features of a uniform flow qualitatively survive, with different onset thresholds. Therefore, the difference between the steady position of the particle centre observed in the glycerine–water mixture and the small precessing motion found in pure water (see § 3) may be caused by what in a uniform flow would be the loss of axial symmetry and onset of unsteadiness. Similarly, the steep fall of the rotational velocity when the Reynolds number exceeds a value of ~650 (to the left of the sharp peak in figure 3) might be due to the collapse and disappearance of the vortex structure which, as argued before, may very well be the 'engine' on which the fast spin relies.

10. Summary

Whereas inertial effects cause a particle to spin more slowly than the fluid in a streamwise shear, we have found that, in the presence of a significant cross-stream shear component of the flow, the particle spins faster than the fluid due to a strong deflection of the wake. Unexpectedly, in the parameter range we have investigated, we found that the spin rates produced by the streamwise and cross-stream shear can be added to give a very close approximation to the spin rate calculated when both shear components are present simultaneously.

Combining the two types of shear into a solid-body rotation gives a result in which the spin rate is larger than that of the ambient fluid. The fact that, in a solid-body rotation, the particle spins faster than the fluid has been confirmed by experiment and simulation. The difference between the influence of the two shear types yields the particle spin rate in a strain flow combined with a uniform flow.

A study of the shear stress on the particle surface suggests the location of the separation lines. In view of the complexity of three-dimensional separation on a moving wall, we have not attempted to determine precisely the position on these lines. We have simply identified the region of low shear stress behind the particle. When a cross-stream shear is present this region moves counterclockwise with respect to the uniform flow. For a rotating particle, the low-shear region to some extent moves back clockwise.

A tentative explanation for the phenomenon is based on the different modifications of the vortex structure behind the sphere caused by the different flows. The cross-stream shear causes a sideways displacement of the vortex structure and a shift in the low-shear region. Since the strength of this vortex increases with Re, so does the effect. This trend abruptly breaks down at $Re \sim 650$, where the particle spin rate starts to decrease until ultimately falling below that of the fluid. We have suggested that this qualitative change may be due to the destabilization and disappearance of the vortex structure behind the sphere.

The particle spin has a clear effect on the lift coefficient in the intermediate-Reynolds-range. We have computed that, in a solid body rotation at $Re = 20$ and 50, the lift coefficient is 47 % and 34 %, respectively, larger for a rotating than for a non-rotating sphere.

We would like to thank Professor S. Balachandar and Professor P. Bagchi for their discussions by correspondence and G. W. H. Bruggert and M. Bos for building the experimental setup. This work is part of the research programs of STW and FOM, which is financially supported by NWO.

REFERENCES

Annamalai, P. & Cole, R. 1986 Particle migration in rotating liquids. *Phys. Fluids* **29**, 647–649.

Auton, T. R. 1987 The lift force on a spherical body in a rotational flow. *J. Fluid Mech.* **183**, 199–218.

Auton, T. R., Hunt, J. C. R. & Prud'homme, M. 1988 The force excerted on a body in inviscid unsteady non-uniform rotating flow. *J. Fluid Mech.* **197**, 241–257.

Bagchi, P. 2002 Particle dynamics in inhomogeneous flows at moderate-to-high Reynolds number. PhD thesis, University of Illinois.

Bagchi, P. & Balachandar, S. 2002*a* Effect of free rotation on the motion of a solid sphere in linear shear flow at moderate *Re*. *Phys. Fluids* **14**, 2719–2737.

Bagchi, P. & Balachandar, S. 2002*b* Shear versus vortex-induced lift force on a rigid sphere at moderate *Re*. *J. Fluid Mech.* **473**, 379–388.

Bagchi, P. & Balachandar, S. 2003 Inertial and viscous force on a rigid sphere in straining flows at moderate Reynolds numbers. *J. Fluid Mech.* **481**, 105–148.

Barkla, H. M. & Auchterlonie, L. J. 1971 The Magnus or Robins effect on rotating spheres. *J. Fluid Mech.* **47**, 437–447.

Bluemink, J. J., van Nierop, E., Luther, S., Deen, N., Magnaudet, J., Prosperetti, A. & Lohse, D. 2005 Asymmetry-induced particle drift in a rotating flow. *Phys. Fluids* **17**, 072106.

Brown, D., Cortez, R. & Minion, M. 2001 Accurate projection methods for the incompressible Navier-Stokes equations. *J. Comput. Phys.* **168**, 196–216.

Bugayevskiy, L. M. & Snyder, J. P. 1995 *Map Projections – A Reference Manual*. Taylor & Francis.

Candelier, F., Angilella, J. R., & Souhar, M. 2004 On the effect of the Boussinesq-Basset force on the radial migration of a stokes particle in a vortex. *Phys. Fluids* **16**, 1765–1776.

Candelier, F., Angilella, J.-R. & Souhar, M. 2005 On the effect of inertia and history forces on the slow motion of a spherical solid or gaseous inclusion in a solid-body rotation flow. *J. Fluid Mech.* **545**, 113–139.

Childress, S. 1964 The slow motion of a sphere in a rotating, viscous fluid. *J. Fluid Mech.* **20**, 305–314.

Clift, R., Grace, J. R. & Weber, M. E. 1978 *Bubbles, Drops and Particles*. Academic.

Coimbra, C. F. M. & Kobayashi, M. H. 2002 On the viscous motion of a small particle in a rotating cylinder. *J. Fluid Mech.* **469**, 257–286.

Dandy, D. S. & Dwyer, H. A. 1990 A sphere in shear flow at finite Reynolds number: effect of shear on particle lift, drag, and heat transfer. *J. Fluid Mech.* **216**, 381–410.

Degani, A. T., Walker, J. D. A. & Smith, F. T. 1998 Unsteady separation past moving surfaces. *J. Fluid Mech.* **375**, 1–38.

Délery, J. M. 2001 Robert Legendre and Henri Werlé: Toward the elucidation of three-dimensional separation. *Annu. Rev. Fluid Mech.* **33**, 129–154.

Dennis, S. C. R., Singh, S. N. & Ingham, D. B. 1980 The steady flow due to a rotating sphere at low and moderate Reynolds numbers. *J. Fluid Mech.* **101**, 257–279.

Dennis, S. C. R. & Walker, J. D. A. 1971 Calculation of the steady flow past a sphere at low and moderate Reynolds numbers. *J. Fluid Mech.* **48**, 771–789.

Drew, D. A. & Lahey, R. T. 1987 The virtual mass and lift force on a sphere in rotating and straining inviscid flow. *Intl J. Multiphase Flow* **13**, 113–121.

Gao, H., Ayyaswamy, P. S. & Ducheyne, P. 1997 Dynamics of a microcarrier particle in the simulated microgravity environment of a rotating-wall vessel. *Microgravity Sci. Technol.* **10**, 154–165.

Ghidersa, B. & Dusek, J. 2000 Breaking of axisymmetry and onset of unsteadiness in the wake of a sphere. *J. Fluid Mech.* **423**, 33–69.

Gotoh, T. 1990 Brownian motion in a rotating flow. *J. Statist. Phys.* **59**, 371–402.

Happel, J. & Brenner, H. 1965 *Low Reynolds Number Hydrodynamics*. Prentice Hall.

Harper, E. Y. & Chang, I-Dee 1968 Maximum dissipation resulting from lift in a slow viscous shear flow. *J. Fluid Mech.* **33**, 209–225.

Herron, I. H., Davis, S. D. & Bretherton, F. P. 1975 On the sedimentation of a sphere in a centrifuge. *J. Fluid Mech.* **68**, 209–234.

Jenny, M., Bouchet, G. & Dusek, J. 2003 Nonvertical ascension or fall of a free sphere in a newtonian fluid. *Phys. Fluids* **15**, L9–L12.

Jenny, M., Dusek, J. & Bouchet, G. 2004 Instabilities and transition of a sphere falling or ascending freely in a newtonian fluid. *J. Fluid Mech.* **508**, 201–239.

Johnson, T. A. & Patel, V. C. 1999 Flow past a sphere up to a Reynolds number of 300. *J. Fluid Mech.* **378**, 19–70.

Kim, D. & Choi, H. 2002 Laminar flow past a sphere rotating in the streamwise direction. *J. Fluid Mech.* **461**, 365–386.

Kim, S. & Karrila, S. 1991 *Microhydrodynamics*. Butterworth-Heinemann.

Kobayashi, M. H. & Coimbra, C. F. M. 2005 On the stability of the Maxey-Riley equation in nonuniform linear flows. *Phys. Fluids* **17**, 113301.

Kurose, R. & Komori, S. 1999 Drag and lift forces on a rotating sphere in a linear shear flow. *J. Fluid Mech.* **384**, 183–206.

Lamb, H. 1932 *Hydrodynamics*, 6th Edn. Dover.

Lee, S. S. 2000 A numerical study of the unsteady wake behind a sphere in a uniform flow at moderate Reynolds numbers. *Comput. Fluids* **29**, 639–667.

Lee, S. S. & Wilczak, J. M. 2000 The effects of shear flow on the unsteady wakes behind a sphere at moderate Reynolds numbers. *Fluid Dyn. Res.* **27**, 1–22.

Lighthill, M. J. 1956 Drift. *J. Fluid Mech.* **1**, 31–53.

Lin, C. J., Peery, J. H. & Schowalter, W. R. 1970 Simple shear flow round a rigid sphere: inertial effects and suspension rheology. *J. Fluid Mech.* **44**, 1–17.

Lohse, D. & Prosperetti, A. 2003 Controlling bubbles. *J. Phys.: Condens. Matter* **15**, S415–S420.

Magnaudet, J., Rivero, M. & Fabre, J. 1995 Accelerated flows past a rigid sphere or a spherical bubble. *J. Fluid Mech.* **284**, 97–135.

McLaughlin, J. B. 1991 Inertial migration of a small sphere in linear shear flows. *J. Fluid Mech.* **224**, 261–274.

Mei, R. 1992 An approximate expression for the shear lift force on a spherical bubble at finite Reynolds number. *Intl J. Multiphase Flow* **18**, 145–147.

Mikulencak, D. R. & Morris, J. F. 2004 Stationary shear flow around fixed and free bodies at finite Reynolds number. *J. Fluid Mech.* **520**, 215–242.

Milne-Thompson, L. M. 1968 *Theoretical hydrodynamics*. Macmillan.

Mortensen, P. H., Andersson, H. I., Gillissen, J. J. J. & Boersma, B. J. 2007 Particle spin in a turbulent shear flow. *Phys. Fluids* **19**, 078109.

Mullin, T., Li, Y., del Pino, C. & Ashmore, J. 2005 An experimental study of fixed points and chaos in the motion of spheres in a stokes flow. *IMA J. Appl. Maths* **70**, 666–676.

Naciri, M. A. 1992 Contribution à l'étude des forces exercées par un liquide sur une bulle de gaz: portance, masse ajoutée et interactions hydrodynamiques. PhD thesis, L'Ecole Central de Lyon.

Natarajan, R. & Acrivos, A. 1993 The instability of the steady flow past spheres and disks. *J. Fluid Mech.* **254**, 323.–344.

van Nierop, E. A., Luther, S., Bluemink, J. J., Magnaudet, J., Prosperetti, A. & Lohse, D. 2007 Drag and lift forces on bubbles in a rotating flow. *J. Fluid Mech.* **571**, 439–454.

Oesterlé, B. & Dinh, T. Bui 1998 Experiments on the lift of a spinning sphere in a range of intermediate Reynolds numbers. *Exps. Fluids* **25**, 16–22.

Paradisi, P. & Tampieri, F. 2001 Stability analysis of solid particle motion in rotational flows. *Nuovo Cimento* C **24c**, 407–420.

Poe, G. G. & Acrivos, A. 1975 Closed-streamline flows past rotating single cylinders and spheres: inertia effects. *J. Fluid Mech.* **72**, 605–623.

Raju, N. & Meiburg, E. 1997 Dynamics of small, spherical particles in vortical and stagnation point flow fields. *Phys. Fluids* **9**, 299–314.

Roberts, G. O., Kornfeld, D. M. & Fowlis, W. W. 1991 Particle orbits in a rotating liquid. *J. Fluid Mech.* **229**, 555–567.

Rubinow, S. I. & Keller, J. B. 1961 The transverse force on a spinning sphere moving in a viscous fluid. *J. Fluid Mech.* **11**, 447–459.

Saffman, P. G. 1965 The lift on a small sphere in a slow shear flow. *J. Fluid Mech.* **22**, 385–400; and Corrigendum, **31**, p. 624 (1968).

Sridhar, G. & Katz, J. 1995 Drag and lift forces on microscopic bubbles entrained by a vortex. *Phys. Fluids.* **7**, 389–399.

Surana, A., Grunberg, O. & Haller, G. 2006 Exact theory of three-dimensional flow separation. Part 1. Steady separation. *J. Fluid Mech.* **564**, 57–103.

Taneda, S. 1978 Visual observations of the flow past a sphere at Reynolds numbers between 10^4 and 10^6. *J. Fluid Mech.* **85**, 178–192.

Thompson, M. C., Leweke, T. & Provansal, M. 2001 Kinematics and dynamics of sphere wake transition. *J. Fluids Struct.* **15**, 575–585.

Tomboulides, A. G. & Orszag, S. A. 2000 Numerical investigation of transitional and weak turbulent flow past a sphere. *J. Fluid Mech.* **416**, 45–73.

Van Dommelen, L. L. & Cowley, S. J. 1990 On the Lagrangian description of unsteady boundary layer separation. Part 1. General theory. *J. Flui Fluid Mech.* **210**, 593–626.

Wang, Y., Lu, X. & Zhuang, L. 2004 Numerical analysis of the rotating viscous flow approaching a solid sphere. *Intl J. Numer. Meth. Fluids* **44**, 905–925.

Wedemeyer, E. H. 1964 The unsteady flow within a spinning cylinder. *J. Fluid Mech.* **20**, 383–399.

Weisenborn, A. J. 1985 Drag on a sphere moving slowly in a rotating viscous fluid. *J. Fluid Mech.* **153**, 215–227.

Williams III, J. C. 1977 Incompressible boundary-layer separation. *Annu. Rev. Fluid Mech.* **9**, 113–144.

Ye, J. & Rocco, M. C. 1992 Particle rotation in a Couette flow. *Phys. Fluids* A **4**, 220–224.

Zhang, Z. & Prosperetti, A. 2005 A second-order method for three-dimensional particle simulation. *J. Comput. Phys.* **210**, 292–324.

Zhang, Z. Z., Botto, L. & Prosperetti, A. 2006 Microstructural effects in a fully-resolved simulation of 1,024 sedimenting spheres. In *IUTAM Symposium on Computational Approaches to Multiphase Flow*, *Fluid Mechanics and Its Applications*, vol. 81.